

# Lithospheric magma dynamics beneath the El Hierro Volcano, Canary Islands: insights from fluid inclusions

E. Ogialoro<sup>1</sup> · M.L. Frezzotti<sup>1</sup> · S. Ferrando<sup>2</sup> · C. Tiraboschi<sup>1</sup> · C. Principe<sup>3</sup> · G. Groppelli<sup>4</sup> · I.M. Villa<sup>1,5,6</sup>

Received: 16 January 2017 / Accepted: 1 September 2017 / Published online: 14 September 2017  
© Springer-Verlag GmbH Germany 2017

**Abstract** At active volcanoes, petrological studies have been proven to be a reliable approach in defining the depth conditions of magma transport and storage in both the mantle and the crust. Based on fluid inclusion and mineral geothermobarometry in mantle xenoliths, we propose a model for the magma plumbing system of the Island of El Hierro (Canary Islands). The peridotites studied here were entrained in a lava flow exposed in the El Yulan Valley. These lavas are part of the rift volcanism that occurred on El Hierro at approximately 40–30 ka. The peridotites are spinel lherzolites, harzburgites, and dunites which equilibrated in the shallow mantle at pressures between 1.5 and 2 GPa and at temperatures between 800 and 950 °C (low-temperature peridotites; LT), as well as at higher equilibration temperatures of 900 to 1100 °C (high-temperature peridotites; HT). Microthermometry and Raman analyses of fluid inclusions reveal trapping of two distinct fluid phases: early type I metasomatic CO<sub>2</sub>-N<sub>2</sub> fluids

( $X_{N_2} = 0.01\text{--}0.18$ ; fluid density ( $d$ ) = 1.19 g/cm<sup>3</sup>), coexisting with silicate-carbonate melts in LT peridotites, and late type II pure CO<sub>2</sub> fluids in both LT ( $d = 1.11\text{--}1.00$  and 0.75–0.65 g/cm<sup>3</sup>) and HT ( $d = 1.04\text{--}1.11$  and 0.75–0.65 g/cm<sup>3</sup>) peridotites. While type I fluids represent metasomatic phases in the deep oceanic lithosphere (at depths of 60–65 km) before the onset of magmatic activity, type II CO<sub>2</sub> fluids testify to two fluid trapping episodes during the ascent of xenoliths in their host mafic magmas. Identification of magma accumulation zones through interpretation of type II CO<sub>2</sub> fluid inclusions and mineral geothermobarometry indicate the presence of a vertically stacked system of interconnected small magma reservoirs in the shallow lithospheric mantle between a depth of 22 and 36 km (or 0.67 to 1 GPa). This magma accumulation region fed a short-lived magma storage region located in the lower oceanic crust at a depth of 10–12 km (or 0.26–0.34 GPa). Following our model, the 40–30-ka-old volcanic activity of El Hierro is related to this mantle-based magma system, a system that we propose fed the recent 2011–2012 eruption.

Editorial responsibility: V.S. Kamenetsky

✉ M.L. Frezzotti  
maria.frezzotti@unimib.it

- <sup>1</sup> Dipartimento di Scienze dell'Ambiente e della Terra, Università di Milano Bicocca, 20126 Milan, Italy
- <sup>2</sup> Dipartimento di Scienze della Terra, Università di Torino, 70125 Turin, Italy
- <sup>3</sup> Istituto di Geoscienze e Georisorse, Consiglio Nazionale delle Ricerche, 56121 Pisa, Italy
- <sup>4</sup> Istituto per la Dinamica dei Processi Ambientali-sezione di Milano, Consiglio Nazionale delle Ricerche, 20131 Milan, Italy
- <sup>5</sup> Institut für Geologie, Universität Bern, 3012 Bern, Switzerland
- <sup>6</sup> Centro Universitario Datazioni e Archeometria, Università di Milano Bicocca, 20126 Milan, Italy

**Keywords** El Hierro · Petrology · Fluid inclusions · Mantle xenoliths · Magma transport

## Introduction

A central question in forecasting eruptive behavior at active volcanic centers is: what is the architecture of the magma plumbing system? (cf. Shaw 1980a, b; Ryan 1987, 1988). This system exerts a critical control on the compositional variation of erupted magmas, as well as the depths and conditions at which they are stored, plus their residence time at different crustal/mantle levels (e.g., Sparks 2003; Peccerillo et al. 2006; Scandone et al. 2007).

A number of complementary studies combining both geophysical and petrological approaches can be used to gain insight into the internal structure of volcanoes (e.g., Bertagnini et al. 2003; Schwarz et al. 2004; Morgan et al. 2007; Stroncik et al. 2009). More specifically, fluid inclusions and mineral geothermobarometry can provide information on the depth of magma ponding and crystallization (c.f. Andersen and Neumann 2001; Frezzotti and Peccerillo 2004; Hansteen and Klügel 2008). Fluid inclusions record pressures of fluid entrapment and changes in fluid density in response to magma pressure variations over short time scales (Peccerillo et al. 2006). They are therefore sensitive records of discrete magma storage regions.

This approach has been successfully applied to active volcanoes both in the oceanic and continental lithosphere (e.g., Hawaii, Canary Islands, Azores, and the Aeolian Islands; Roedder 1983; De Vivo et al. 1988, Frezzotti et al. 1991; Hansteen et al. 1998; Zanon et al. 2003; Zanon and Frezzotti 2013). In the Canary Islands, previous fluid inclusion studies suggested that the volcanoes' plumbing system transports magma directly to the lower crust (e.g., Hansteen et al. 1991, 1998; Frezzotti et al. 1994; Andersen et al. 1995; Neumann et al. 1995; Viti and Frezzotti 2000; Klügel et al. 2005, 2015). Although fluid inclusion investigations have failed to identify magma storage regions below the Moho, mineral-melt geothermobarometry indicates variable clinopyroxene crystallization from 15 to 45 km depth beneath La Palma and El Hierro (Stroncik et al. 2009; Barker et al. 2015; Klügel et al. 2015).

Multidisciplinary research carried out following the last submarine eruption of El Hierro in 2011–2012 has identified the presence of two discrete magma storage regions located in the lower oceanic crust and the lithospheric mantle (Meletlidis et al. 2012; Becerril et al. 2013b; González et al. 2013; Martí et al. 2013a, b; Longpré et al. 2014; Klügel et al. 2015; Carracedo et al. 2015; Zaczek et al. 2015). As summarized by Klügel et al. (2015), magma transport in the oceanic crust is characterized by sub-horizontal and lateral pathways forming temporary deep sheet intrusions (sills). These are fed by a deeper reservoir in the shallow lithospheric mantle. However, the nature of this sub-Moho magma storage region has not been fully resolved (e.g., Martí et al. 2013a).

In this work, we concentrate on the reconstruction of the magma plumbing system of the El Hierro Volcano, focusing on magma storage in the oceanic lithospheric mantle. Following the approach of Frezzotti and Peccerillo (2004), we performed geothermobarometry on fluid inclusions and minerals in ultramafic xenoliths from a lava flow located in the El Julan cliff, representative of rift volcanism activity (approximately 40–30 ka; Guillou et al. 1996; Carracedo et al. 2001; Becerril et al. 2013a). The results allow us to model the internal structure of the El Hierro Volcano.

## Geological setting

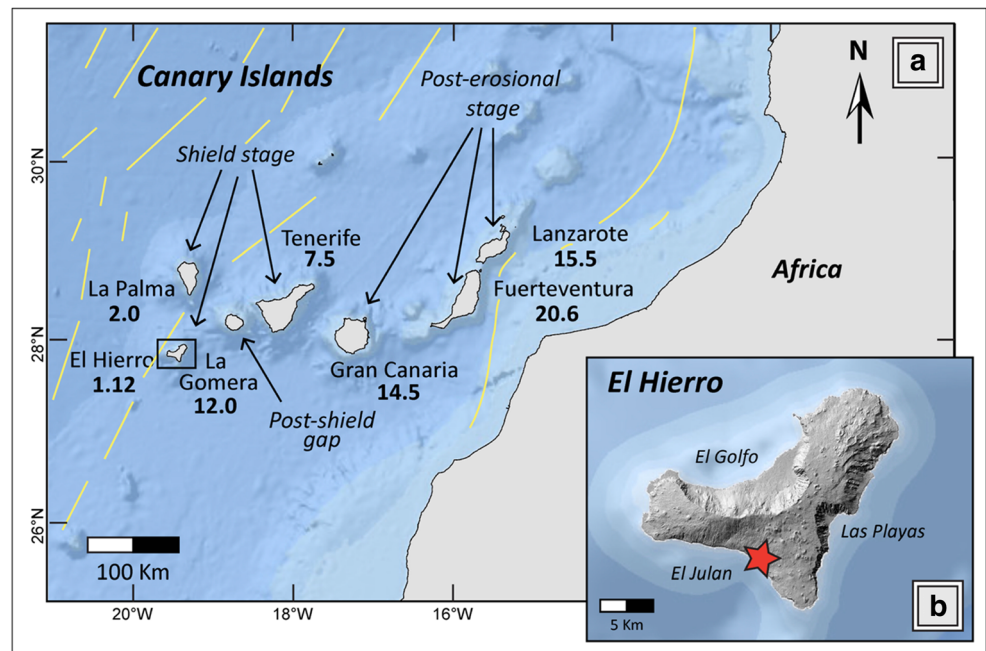
The Canary Islands archipelago (Spain) consists of seven main volcanic islands located on the continental rise off Cape Juby (northwest Africa). It extends for roughly 500 km along a ridge which originates on the margin of the African Plate (Fig. 1a) (Robertson and Stillman 1979; Marinoni and Pasquaré 1994; Carracedo 1999; Marinoni and Gudmundsson 2000).

The sub-aerial volcanic activity shows a general decrease in age westwards from 21 to 20 Ma at Fuerteventura-Lanzarote to less than 2 Ma at El Hierro and La Palma (Fig. 1a); the latter are currently in their shield building phase (Schmincke 1982; Guillou et al. 1996; Carracedo 1999). The islands lay on oceanic lithosphere formed during the opening of the Central Atlantic Ocean (~ 150–180 Ma; Hoernle 1998). The oceanic crust also shows a progressive thinning westward, from about 35 km at Lanzarote (Martinez-Arevalo et al. 2013) to 12–15 km at El Hierro. The main regional tectonic structures have been classified as “oceanic” in the Atlantic (N160–N180° E, N120–N135° E) and “continental” nearer to Africa (N20° E, N45° E, N75° E) (Anguita and Hernán 1975, 2000; Fuster 1975; Geyer and Martí 2010).

Magmatic activity is dominated by alkali-basalts (picrites, basanites), with minor tholeiites and differentiated lavas (e.g., trachytes and phonolites). The origin of intraplate volcanic activity is still controversial (cf. Lustrino and Wilson 2007). The most popular genetic hypothesis is the mantle plume model (e.g., Hoernle and Schmincke 1993; Carracedo et al. 1998; Duggen et al. 2009), although other interpretations have been proposed, including a local extensional model (Fuster 1975) and an uplifted tectonic block model (Araña and Ortiz 1991). Anguita and Hernán (2000) postulated a single unified model taking into account mantle plume dynamics combined with the regional tectonics to explain the initiation of mantle melting.

At El Hierro, sub-aerial volcanic activity started at 1.12 Ma, with massive lava flows in the NE of the island (Guillou et al. 1996). Three main volcanic cycles have been identified, namely the Tiñor Edifice (1.12–0.88 Ma), the Golfo-Las Playas Edifice (0.545–0.176 Ma), and Rift Volcanism (0.158 Ma–present) (Carracedo et al. 2001; IGME 2010a, b, c, d; Becerril et al. 2013a). These cycles are separated by quiescence, structural deformation, and sector collapses. Sector collapses have formed four main amphitheatres: Las Playas I and II (~ 545–0.176 and 0.176–0.145 Ma, respectively), El Julan (~ 0.158 Ma), and the Golfo (~ 87–39 ka) (Masson 1996; Masson et al. 2002, 2006; Gee et al. 2001; Longpré et al. 2011). Erupted lavas increase in alkalinity and degree of evolution through time (Stroncik et al. 2009). Lavas from the Tiñor Volcano are picritic to hawaiitic-tephritic in composition, whereas those of the Golfo-Las Playas edifice range from basanites to trachytes and nephelinites.

**Fig. 1** **a** Geographical setting of the Canary Islands showing the age of the volcanism and the stages of growth (shield stage, post-erosional stage, post-shield gap) (modified from Carracedo 1999, Acosta et al. 2005). The yellow lines define the main structures of Atlantic and African tectonic units. Numbers below each island name give the age in ka. **b** Geographical setting of El Hierro Island showing xenolith sampling locality in El Julian cliff Valley (red star)



The last cycle, Rift Volcanism (158 ka–present), is characterized by cinder cones and relatively thin lava flows covering most of the island. Lavas are mainly alkali-picrites and basanites with minor tephrites (Carracedo et al. 2001). Radiometric ages ranging from 158 to 2.5 ka broadly constrain the Rift Volcanism activity (Guillou et al. 1996; Carracedo et al. 2001). Only one eruption has occurred in the last 600 years: a single submarine monogenic eruption in the La Restinga area in 2011–2012 (e.g., López et al. 2012; Martí et al. 2013a, b; Longpré et al. 2014).

Abundant ultramafic xenoliths are reported in several lava flows and pyroclastic rocks on El Hierro (Neumann 1990, Hansteen et al. 1991; Neumann et al. 2004). For the present study, xenolith samples were collected from the El Julian Cliff Valley (27° 41' 27" N–18° 02' 49" W), which has not been sampled previously (Fig. 1b). The outcrop consists of a massive basaltic lava flow about 3 m in thickness (Fig. 2a), which is part of a continuous succession with no significant unconformity. No dates are available for this particular xenolith-bearing lava flow, but its position is compatible with the Rift Volcanism activity at approximately 40–30 ka. In addition, Carracedo et al. (2001) dated two lava flows in this area (~ 1 km southwest) at 41 and 31 ka, respectively (K-Ar dating).

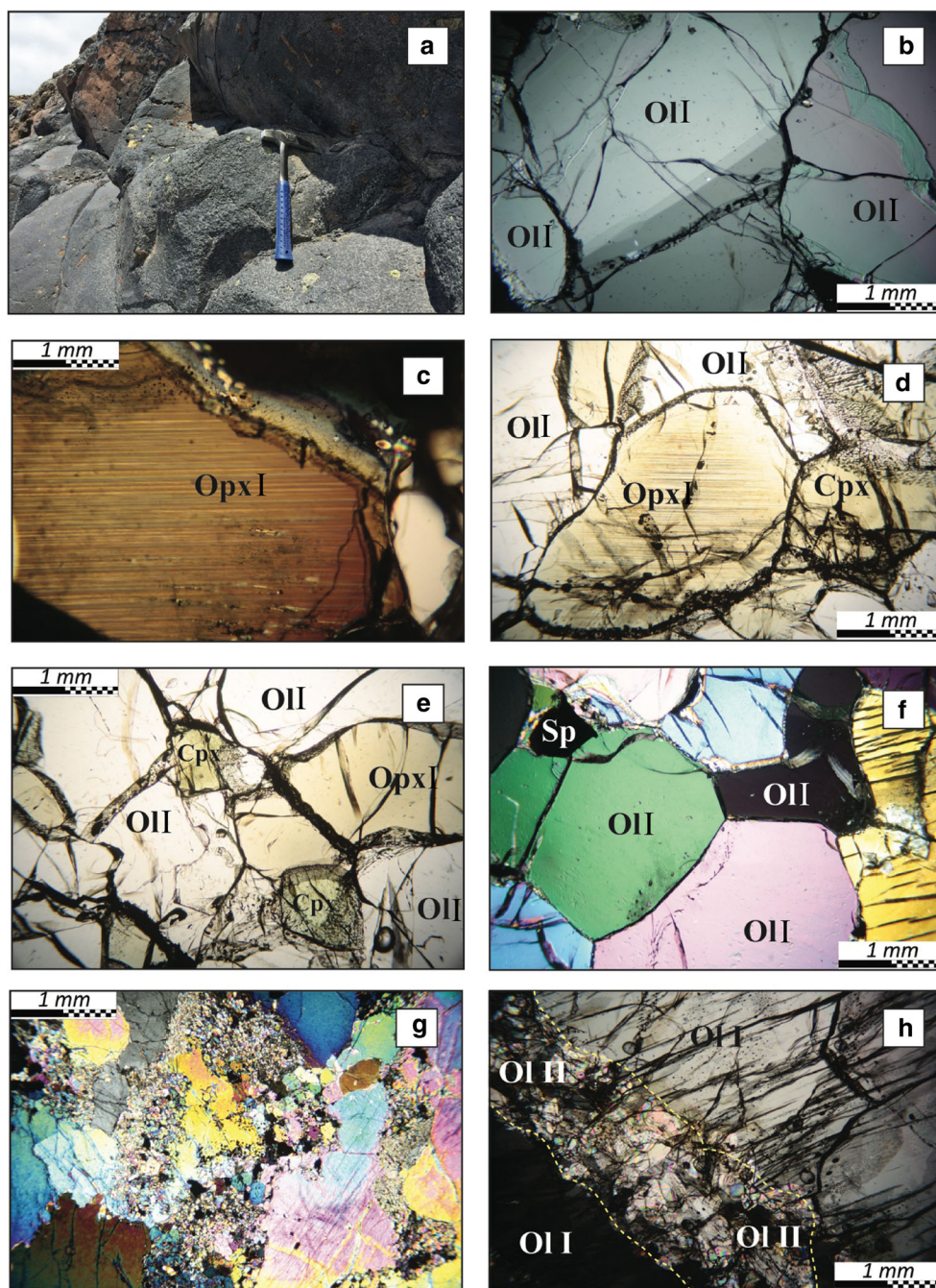
## Analytical techniques

Peridotite modal compositions have been defined by multicolor image analysis (ImageJ and Photoshop C5 softwares), reconstructing the total pixel areas of minerals identified in thin sections.

A wavelength dispersive system (WDS) microprobe was used for major element composition of mineral phases, using double-polished thick sections. WDS analyses were performed with a JEOL JXA 8200 Superprobe, equipped with five wavelength dispersive spectrometers, energy dispersive X-ray spectroscopy (EDS), and cathodoluminescence detectors at the University of Milan. The operating conditions consisted of an acceleration voltage of 15 kV, at a beam current of 15 nA at 30 s counting time, with a spot size of 1  $\mu$ m. The typical detection limit for each element was 0.01%. Natural and synthetic minerals were used as standards, within 2% at  $2\sigma$  standard deviation. Structural formulae of minerals were processed using the NORM software of Ulmer (1986).

Fluid inclusion microthermometry was carried out with a Linkam THMS600 heating/freezing stage, equipped with a Leitz microscope (40 $\times$  objective), which operates in a temperature range between – 196 and 600  $^{\circ}$ C at the University of Milano Bicocca. The instrument was calibrated checking CO<sub>2</sub> and H<sub>2</sub>O triple points (– 56.6 and 0.1  $^{\circ}$ C, respectively) in natural and synthetic fluid inclusions (SYN-FLINC). An accuracy of  $\pm$  0.1  $^{\circ}$ C was estimated in the temperature interval from – 90 to 31  $^{\circ}$ C at the standard reference points, and of  $\pm$  0.2  $^{\circ}$ C at other temperatures. The melting temperature ( $T_m$ ) and the homogenization temperature ( $T_h$ ) of fluid inclusions were measured with a heating rate varying from 0.3 to 0.1  $^{\circ}$ C/min. The density of CO<sub>2</sub> inclusions was calculated using the equation of Duschek et al. (1990) (BULK software; Bakker 2003). Isochores were determined using the equation of Holloway (1981) (ISOCHORE software; Bakker 2003). The selected equation is valid up to least 2000 K and 1.5 GPa. Molar volumes of CO<sub>2</sub>-N<sub>2</sub> fluids were derived by plotting fluid composition, determined by

**Fig. 2** **a** Ultramafic xenoliths in the basaltic lava outcrop of El Julan cliff Valley. **b–h** Microphotographs of studied peridotites. **b** Deformed olivine porphyroclasts (Ol I) in spinel harzburgite (XML9, crossed polarizers). **c** Orthopyroxene porphyroclasts (Opx I) with exsolution lamellae of clinopyroxene (Cpx) in spinel lherzolite (XML8, crossed polarizers). **d** Exsolved Opx I with rims free of exsolution lamellae in spinel harzburgite (XML7, parallel polarizers). **e** Opx I without exsolution lamellae in spinel harzburgite (XML4, parallel polarizers). **f** Olivine neoblasts (Ol II) forming triple junctions in spinel harzburgite XML7, crossed polarizers. **g** Neoblast assemblage of Ol II + Opx II + Cpx + Sp in spinel lherzolite (XML3, crossed polarizers). **h** Ol II forming narrow alignments cutting Ol I in spinel dunite (broken yellow lines) (XML1, crossed polarizers)



Raman spectroscopy, and temperatures of measured sequences of phase transitions in the isochoric ( $\text{cm}^3/\text{mol}$ )  $\text{CO}_2\text{-N}_2$  T-X diagram of van den Kerkhof (1988) and Klemd et al. (1992). Isochores for  $\text{CO}_2\text{-N}_2$  fluid inclusions were calculated using the equation of Holloway (1977), which is valid from 373 to 1273 K and up to 2 GPa (ISOCHORE software; Bakker 2003).

Fluid inclusions were also analyzed by Raman microspectroscopy (Horiba Labram HR800) at the “G. Scansetti” Center of the University of Turin. A polarized Nd green laser operating at 532 nm wavelength and 80 mW

emission power was used as the excitation source, with a spot size resolution of  $1 \times 1 \times 3 \mu\text{m}$ . The slit width was  $300 \mu\text{m}$ , the grating was 600 grooves/mm, and the corresponding spectral resolution was  $\pm 1.5 \text{ cm}^{-1}$ . Raman spectra were collected with a  $100\times$  Olympus objective and three accumulations of 30 s. The calibration of the instrument has been checked daily using the  $521 \text{ cm}^{-1}$  silicon band. Determination of the relative molar fractions of end-member components in  $\text{CO}_2\text{-N}_2$  mixtures, as well as the characterization of daughter minerals in fluid inclusions was carried out following Frezzotti et al. 2012; (and references therein). Spectra statistical fitting was performed

with the Fityk 0.9.8 free analysis software, applying PseudoVoigt functions.

The “Raman densimeter” (e.g., Rosso and Bodnar 1995) for pure CO<sub>2</sub> fluid inclusions, based on the distance of the CO<sub>2</sub> Fermi doublet ( $\Delta$ , in cm<sup>-1</sup>; Wang and Wright 1973; Garrabos et al. 1980) was applied using the equation of Kawakami et al. (2003) with an accuracy of better than 5% in the density range from 0.1 to 1.24 g/cm<sup>3</sup>. Selection of the Raman densimeter equation was performed comparing CO<sub>2</sub> density values derived from microthermometry with those calculated by Raman analyses applying existing empirical equations (cf., Frezzotti et al. 2012) in 20 fluid inclusions. The equation of Kawakami et al. (2003) was found to be the most accurate for studied fluid inclusions.

### Composition and P-T equilibration conditions of peridotites

Ultramafic xenoliths are angular in shape and about 8–10 cm in width on average (Fig. 2a). They are pale green in color, which is characteristic of fresh peridotites. The rock contacts are sharp and lava infiltrations are generally absent. The host basanite lava is unaltered, is porphyritic, and consists of olivine and Ti-augite phenocrysts (30 vol%) in a glassy groundmass. Eleven peridotites were selected for petrological and fluid inclusion studies.

### Petrography and mineral chemistry of peridotites

The samples studied are type I peridotites (Frey and Prinz 1978) and consist of three spinel dunites (Ol 92–94, Cpx 1–4, Opx 4–6 vol%; samples XML 1, 5, and 10), three spinel lherzolites (Ol 63–78, Cpx 11–12, Opx 11–26 vol%; samples XML 3, 6, and 8), and five spinel harzburgites (Ol 59–78, Cpx 2–4, Opx 18–38 vol%; samples XML 4, 7, 9, 11, and 12). Most harzburgites and lherzolites have protogranular textures, with 10 to 30 vol% recrystallization, and only one lherzolite (XML 3) grades into the porphyroclastic type. Reaction rims between xenoliths and host basanite are not observed. Some peridotites contain intragranular or intergranular glass microveins which do not reach the contact with the host lava.

Olivine and orthopyroxene are present as strained porphyroclasts (4–25 mm in size) and smaller polygonal strain-free neoblasts ( $\leq 2$  mm in length). Olivine porphyroclasts (Ol I) are typically coarse grained, with several grains up to 25 mm in length. They show kink-bands (Fig. 2b) and may contain trails of spinel inclusions. Orthopyroxene porphyroclasts (Opx I) are similar in length. In less recrystallized protogranular harzburgites and lherzolites (about 10–20 vol% neoblasts), they show clinopyroxene  $\pm$  spinel exsolution lamellae (Fig. 2c). In more recrystallized protogranular peridotites and in the porphyroclastic

lherzolite, Opx I shows clear rims (Fig. 2d) or does not contain exsolution lamellae (Fig. 2e).

Olivine and orthopyroxene neoblasts (Ol II and Opx II) occur as interstitial grains or as aggregates of polygonal grains showing triple junctions. They are strain-free and may include minute spinel grains (Fig. 2f). In spinel dunites, Ol II grains are distributed along preferred orientations, showing a rock foliation cutting large Ol I (Fig. 2h). Clinopyroxene and spinel have smaller sizes on average (1 mm) than Ol I and Opx I and occur both as subhedral and as interstitial grains. They may form symplectites with orthopyroxene and olivine (Fig. 2g).

In spinel harzburgites and lherzolites, olivine has a narrow Mg# ( $\text{Mg\#} = (\text{Mg}/\text{Mg} + \text{Fe}_{\text{tot}})$ ) ranging from 0.89 to 0.91, with slightly higher values in harzburgites. CaO content varies from 0.01 to 0.17 wt% and NiO from 0.31 to 0.48 wt%. No significant chemical variation between porphyroclasts and neoblasts has been observed, except for a higher CaO content (up to 0.17 wt%, in neoblasts). Opx I and Opx II also show a similar and narrow Mg# interval, from 0.90 to 0.91. Al<sub>2</sub>O<sub>3</sub> content ranges from 2.1 to 3.7 wt%, Cr<sub>2</sub>O<sub>3</sub> from 0.24 to 0.7 wt%, and CaO from 0.36 to 0.81. TiO<sub>2</sub> content is very low ( $< 0.17$  wt%). Clinopyroxene is Cr-diopside with Mg# ranging from 0.89 to 0.93. Cr<sub>2</sub>O<sub>3</sub> varies from 0.48 to 1.1 wt%, and Al<sub>2</sub>O<sub>3</sub> ranges from 1.68 to 4.55 wt% and TiO<sub>2</sub> from 0 to 1.25 wt%. Spinel is a magnetite-spinel solid solution with a Cr# [ $\text{Cr\#} = \text{Cr}/(\text{Cr} + \text{Al})$ ] variable from 0.25 to 0.35. Cr<sub>2</sub>O<sub>3</sub> content ranges from 20.84 to 28.98 wt% and TiO<sub>2</sub> from 0 to 0.22 wt%. Chromite-rich rims (Cr# = 0.4–0.5) are observed around some grains.

### Mineral geothermobarometry

Equilibration temperatures for peridotites were estimated considering the partitioning of Fe<sup>2+</sup>, Mg, and Ca between orthopyroxene and clinopyroxene (Wells 1977; We), the two-pyroxene and the Ca-in-opx thermometers (Brey and Köhler 1990; BK2px and BKopx), and the solubility of Ca and Al in orthopyroxene in equilibrium with olivine, clinopyroxene, and spinel (Witt-Eickschen and Seck 1991; WS). Temperature estimates were performed on exsolved porphyroclasts cores and on clear porphyroclasts and neoblasts of harzburgites and lherzolites.

Exsolved Opx I porphyroclasts provide equilibration temperatures of between 800 and 950 °C. The BK2px thermometer provides the lowest equilibration temperatures at 800 °C, while the We and BKopx thermometers give consistent temperatures ranging from 800 to 920 °C. The WS thermometer provides the highest estimates, with temperatures reaching 950 °C. Clear Opx I thermometry yields higher temperatures with respect to the exsolved porphyroclast thermometry, ranging from 900 to 1100 °C. The BK2px thermometer again provides the lower estimates with temperatures of approximately 900 °C. The We and BK opx thermometers yield more

elevated T conditions of up to 980 °C. The WS thermometer gives the higher equilibration temperatures, from 950 to 1100 °C. Temperature estimates in neoblasts show that peridotites from El Hierro have been locally heated to  $T > 1100$  °C (We and BK thermometers).

From petrography and mineral geothermometry, it is possible to distinguish two groups of peridotites: a first group consists by harzburgites and lherzolites that present exsolved Opx I porphyroclasts, which show equilibration temperatures from 800 to 950 °C (LT peridotites; XML 7, 8, 10, and 11). A second group corresponds to harzburgites and lherzolites that contain clear Opx I porphyroclasts and higher equilibration temperatures from 900 to 1100 °C (HT peridotites; XML 3, 4, 5, and 9). Peridotites from El Hierro and the other Canary Islands have already revealed a bimodal temperature distribution, within the same temperature intervals (e.g., Neumann et al. 2002; i.e., HEXO and HTR peridotites).

Pressures were estimated employing the Koehler and Brey (1990); KB geobarometer, which takes into consideration the diffusion of calcium in olivine. The minimum equilibration pressures correspond to 1.5 GPa, while the maximum conditions reach pressures of 2 GPa. It has to be noted, however, that the KB barometer is strongly temperature dependent; consequently, these pressure estimates are subject to a significant uncertainty.

## Fluid inclusion studies

### Petrography of fluid inclusions

Nine representative samples of LT and HT peridotites were selected for fluid inclusion analysis. They consist of three dunites (XML 1, 5, and 10), four harzburgites (XML 4, 7, 9, and 11), and two lherzolites (XML3 and 9). Fluid inclusions are present in Ol I, Opx I, and clinopyroxene and are more abundant in LT peridotites. Neoblasts of Ol II and Opx II do not contain fluid inclusions.

Two main fluid inclusion assemblages (Roedder 1984; Bodnar 2003) occur. Early type I fluid inclusions are present only in Ol I and exsolved Opx I of LT peridotites (Fig. 3). Inclusions have rounded or negative-crystal shapes and sizes from  $\leq 3$   $\mu\text{m}$  to 50  $\mu\text{m}$  in length. They occur either in small, spatially isolated clusters or as short intragranular trails often along preferred crystallographic orientations (Fig. 3a–c). Type I inclusions are often associated with carbonate-rich inclusions and glass veins (Fig. 3b).

At room temperature, inclusions are CO<sub>2</sub>-rich and single phase (L; Fig. 3c), or they can contain several daughter minerals (i.e., carbonates, or carbonates + sulfates  $\pm$  chlorides  $\pm$  phosphates) and an opaque mineral (two-phase L + S inclusions; Fig. 3a, d). The composition of the daughter mineral phases was determined by Raman microspectroscopy

mapping (Fig. 4a). Carbonates are dolomite, or Mg-calcite and magnesite; sulfates include anhydrite, sulfohalite, and MgSO<sub>4</sub> $\cdot$ xnH<sub>2</sub>O; phosphate is apatite; the opaque phase is either spinel, magnetite, or hematite (Fig. 4b–f).

The second fluid inclusion assemblage is represented by late type II CO<sub>2</sub> fluid inclusions. Type II inclusions were trapped at later stages in Ol I, Opx I, and clinopyroxene of both LT and HT peridotites. They occur as intragranular and intergranular trails of variable length and as isolated clusters (Fig. 5a, c). In exsolved Opx I, type II inclusions are observed along preferential crystallographic orientations (e.g., 010; Fig. 5d). Inclusions have negative-crystal or rounded shapes and sizes ranging from less than 1 to 40  $\mu\text{m}$  in length (Fig. 5b). At room temperature, they are single phase CO<sub>2</sub> (L) or, less commonly, two-phase inclusions (L + V; Fig. 5) and do not contain daughter minerals. Decrepitation textures are frequently observed, particularly in HT peridotites (Fig. 5b, d).

### Composition and density of fluid phases

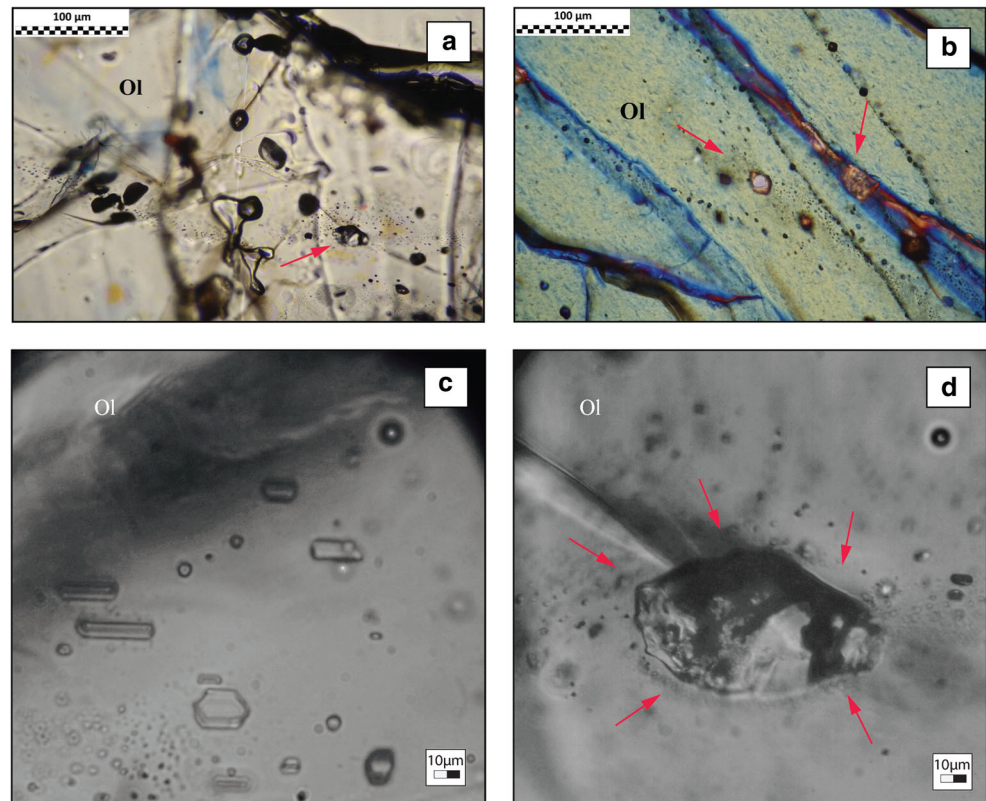
The chemical composition and the density of type I and II fluid inclusions was determined by microthermometry and Raman microspectroscopy. For type II inclusions less than 3  $\mu\text{m}$  in size, the density was calculated using the “Raman densimeter” (Kawakami et al. 2003).

#### Type I fluid inclusions

Phase transitions were observed in 15 single-phase (L) type I inclusions of two LT peridotites in the temperature range from  $-190$  to 20 °C. On cooling, 14 inclusions froze at temperatures of  $-95$  to  $-80$  °C. On subsequent heating, inclusions showed slow melting of solid CO<sub>2</sub>, in a 2–3 °C interval, with initial melting (Ti) recorded at about  $-60$  °C, and final melting (Tm) from  $-58.6$  to  $-56.9 \pm 0.1$  °C (Fig. 6). Homogenization temperatures to the liquid phase (ThL) ranged from  $-52.0$  to  $8.0 \pm 0.1$  °C. According to the classification of van den Kerkhof (1988), these phase transitions (Ti; S + L  $\rightarrow$  S + L + V, Tm; S + L + V  $\rightarrow$  L + V, ThL; SL + V  $\rightarrow$  L) identify H3 type CO<sub>2</sub>-rich inclusions containing minor additional gaseous species.

One type I inclusion ( $\sim 10$   $\mu\text{m}$  in size, red arrow in Fig. 7a) shows different microthermometric behavior. On cooling down to  $-190$  °C, solid CO<sub>2</sub> nucleation occurred in the presence of liquid and vapor phases (L + S + V). On heating, four subsequent phase transitions were recorded. Partial homogenization in the presence of solid CO<sub>2</sub> (ThS; S + L + V  $\rightarrow$  S + L) occurred at about  $-152$  °C; then a small bubble reappeared at  $-95$  °C (Ti; S + L  $\rightarrow$  S + L + V). On further heating, the partial homogenization in the presence of solid CO<sub>2</sub> (ThS; S + L + V  $\rightarrow$  S + L) was measured at  $-61.0 \pm 0.1$  °C. The last phase transition took place by dissolution of solid CO<sub>2</sub> (Ts; S + L  $\rightarrow$  L) in a one-phase liquid-

**Fig. 3** Microphotographs of early type I fluid inclusions in low-temperature (LT) peridotites. **a** Intragranular trail of type I fluid inclusions in OI I (harzburgite XML7, parallel polarizers). **b** Carbonate (high birefringency) in fluid inclusions and microveins (red arrows) in OI I (harzburgite XML7, crossed polarizers). **c** Cluster of type I fluid inclusions in Opx I (harzburgite XML7, parallel polarizers). **d** multiphase type I fluid inclusion containing several daughter minerals and showing evidence for partial decrepitation (red arrows in OI I (harzburgite XML7 parallel polarizers)



like fluid at  $-60.0 \pm 0.1$  °C. According to van den Kerkhof (1988), this sequence of phase transitions (S4 type fluid inclusions) identifies extremely dense  $\text{CO}_2\text{-N}_2$  mixtures.

In all analyzed type I inclusions, the presence of nitrogen was confirmed by the  $\text{N}_2$  band from  $2328$  to  $2330$   $\text{cm}^{-1}$  in the Raman spectra (Fig. 7 b, c). An  $\text{N}_2$  molar fraction ( $X_{\text{N}_2}$ ) of 0.18 was calculated for the S4-type  $\text{CO}_2\text{-N}_2$  inclusion by quantitative Raman analysis (red arrow in Fig. 7 a). H3-type inclusions contain less  $\text{N}_2$ , being  $X_{\text{N}_2}$  comprised between 0.05 and 0.09 (Fig. 7 a). The molar volume of  $\text{CO}_2\text{-N}_2$  mixtures was derived by plotting the measured sequence of phase transitions in the  $\text{CO}_2\text{-N}_2$  T-X isochoric ( $\text{cm}^3/\text{mol}$ ) diagram (Fig. 8) of van den Kerkhof (1988) and Klemm et al. (1992). For the S4-type inclusion ( $X_{\text{N}_2} = 0.18$  and  $T_{\text{hs}} = -152$  °C), the corresponding molar volume is  $34.5$   $\text{cm}^3/\text{mol}$  (i.e., density ( $d$ ) =  $1.19$   $\text{g}/\text{cm}^3$ ). For H3-type inclusions, molar volumes range from  $38.5$   $\text{cm}^3/\text{mol}$  ( $X_{\text{N}_2} = 0.05\text{--}0.09$  and  $T_{\text{hL}}$  from  $-52$  to  $-51$  °C) to  $40\text{--}50$   $\text{cm}^3/\text{mol}$  ( $X_{\text{N}_2} = 0.01$  and  $T_{\text{hL}}$  from  $-35$  to  $8$  °C) (Figs. 7 a and 8).

#### Type II fluid inclusions

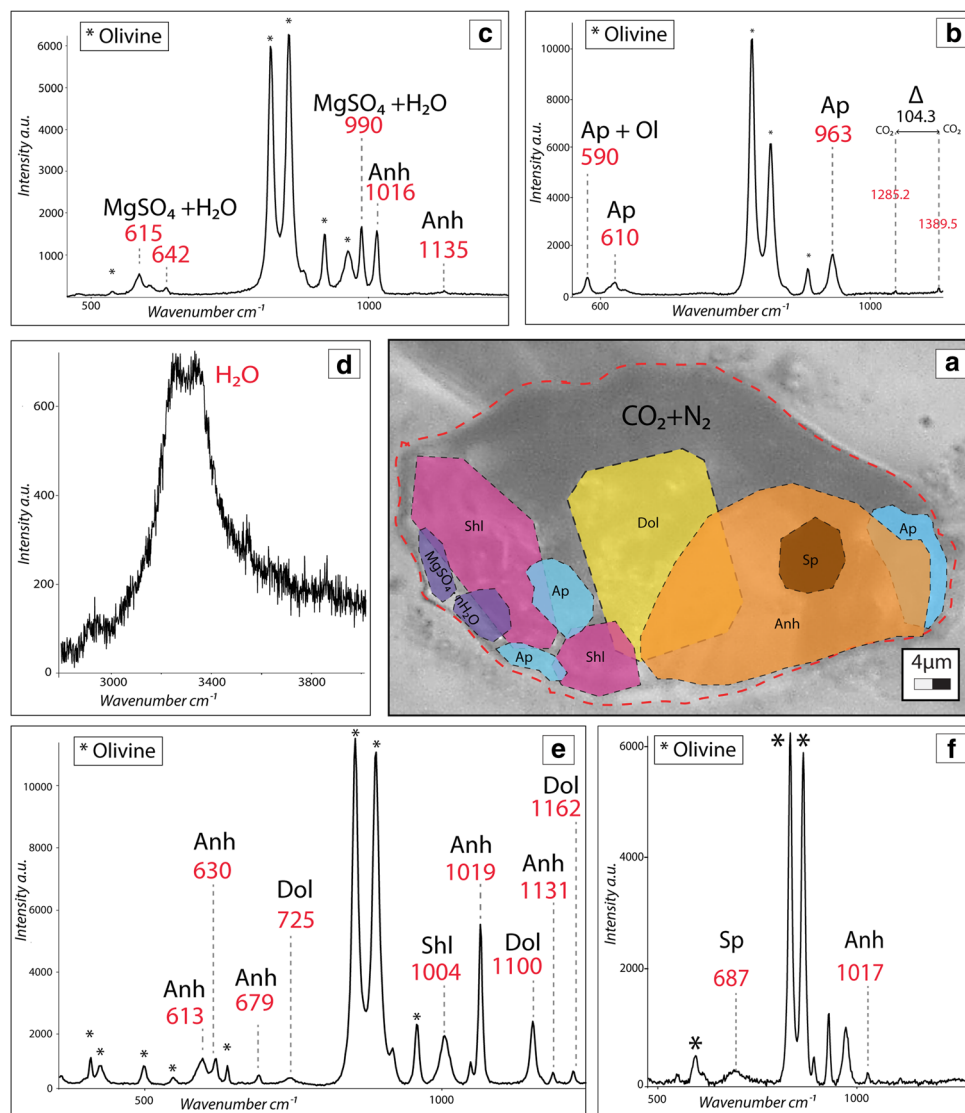
On cooling, type II  $\text{CO}_2$  fluid inclusions froze at temperatures of  $-95$  to  $-65$  °C. Solid  $\text{CO}_2$  melted instantaneously from  $-57.3$  to  $-56.5 \pm 0.1$  °C ( $T_{\text{m}}$ ;  $n = 50$ ), with most measurements at  $-56.6$  °C (Fig. 6). Melting behavior indicates that fluid inclusions consist of pure  $\text{CO}_2$ , as confirmed by Raman

analysis. Liquid water and/or clathrates were not observed in any of the measured inclusions by either analytical technique.

Type II pure  $\text{CO}_2$  inclusion homogenization occurred to the liquid phase ( $T_{\text{hL}}$ ;  $n = 512$ ) with a scattered distribution from  $-37.5$  to  $31.0 \pm 0.1$  °C (Fig. 9). Only 2% of the analyzed inclusions had homogenization to the vapor phase (not shown). When  $T_{\text{hL}}$  values are plotted separately for inclusions in LT and HT peridotites, measurements define two frequency intervals at slightly different temperatures (Fig. 10). In LT peridotites, the two frequency intervals range from  $-37.5$  to  $-12$  °C and from  $20$  to  $31$  °C, respectively (Fig. 10 a). In HT peridotites, the first  $T_{\text{hL}}$  distribution interval occurs at slightly higher temperatures, from  $-24$  to  $0$  °C, while the latter occurs in the same interval from  $20$  to  $31$  °C (Fig. 10 b). Corresponding  $\text{CO}_2$  density values range between  $1.11$  and  $0.99 \pm 0.01$   $\text{g}/\text{cm}^3$  and  $0.75$  and  $0.65 \pm 0.01$   $\text{g}/\text{cm}^3$  in LT peridotites and between  $1.04$  and  $0.91 \pm 0.01$   $\text{g}/\text{cm}^3$  and  $0.75$  and  $0.65 \pm 0.01$   $\text{g}/\text{cm}^3$  in HT peridotites.

As a general rule of thumb, the preservation of a fluid inclusion depends on both inclusion size and on the mechanical properties of the enclosing mineral (e.g., Bodnar et al. 1989; Campione et al. 2015). For this reason, the distribution of  $T_{\text{hL}}$  measurements for type II  $\text{CO}_2$  inclusions was also investigated in the different mineral phases. As shown by the histograms in Fig. 11,  $T_{\text{hL}}$  distribution is similar in orthopyroxene and clinopyroxene where the lowest  $T_{\text{hL}}$  values correspond to a density of  $1.11 \pm 0.1$   $\text{g}/\text{cm}^3$ .

**Fig. 4** Raman characterization of daughter mineral phases in a single type I fluid inclusion. **a** Photomicrograph showing distribution of daughter mineral phases in inclusion based on Raman mapping: anhydrite (Anh), dolomite (Dol), sulfosalite (Shl),  $\text{MgSO}_4 \times n \text{H}_2\text{O}$ , apatite (Ap), spinel (Sp), and  $\text{CO}_2 + \text{N}_2$  fluid. **b–f** Raman spectra of daughter mineral phases: **b** apatite; **c** anhydrite; **d** water in  $\text{MgSO}_4 \times n \text{H}_2\text{O}$ ; **e** anhydrite, sulfosalite, and dolomite; **f** spinel and anhydrite. Red numbers in spectra report Raman modes of identified phases in  $\text{cm}^{-1}$ . Asterisks indicate host mineral vibrations



Conversely, in olivine, ThL's are systematically higher, resulting in lower  $\text{CO}_2$  densities which do not exceed  $1.0 \pm 0.1 \text{ g/cm}^3$ . Therefore, measured type II inclusions in olivine have not preserved fluid density at trapping P-T conditions.

To test if partial decrepitation and/or stretching in olivine was dependent on inclusion size, the densities of 37 inclusions with length  $\leq 3 \mu\text{m}$  were calculated by applying the Raman densimeter of Kawakami et al. (2003). In Raman spectra, measured distances of the  $\text{CO}_2$  Fermi doublet ( $\Delta$ ) from 105.17 to  $104.46 \pm 0.03 \text{ cm}^{-1}$  correspond to  $\text{CO}_2$  densities between 1.11 and  $0.85 \pm 0.1 \text{ g/cm}^3$  (Fig. 12a). This density interval is similar to that obtained by microthermometry in larger  $\text{CO}_2$  inclusions in orthopyroxene and clinopyroxene (Fig. 12a). Thus, data indicate a greater tendency of fluid inclusions in olivine to decrepitate than those in pyroxenes, probably due to mechanical failure on decompression from mantle depths.

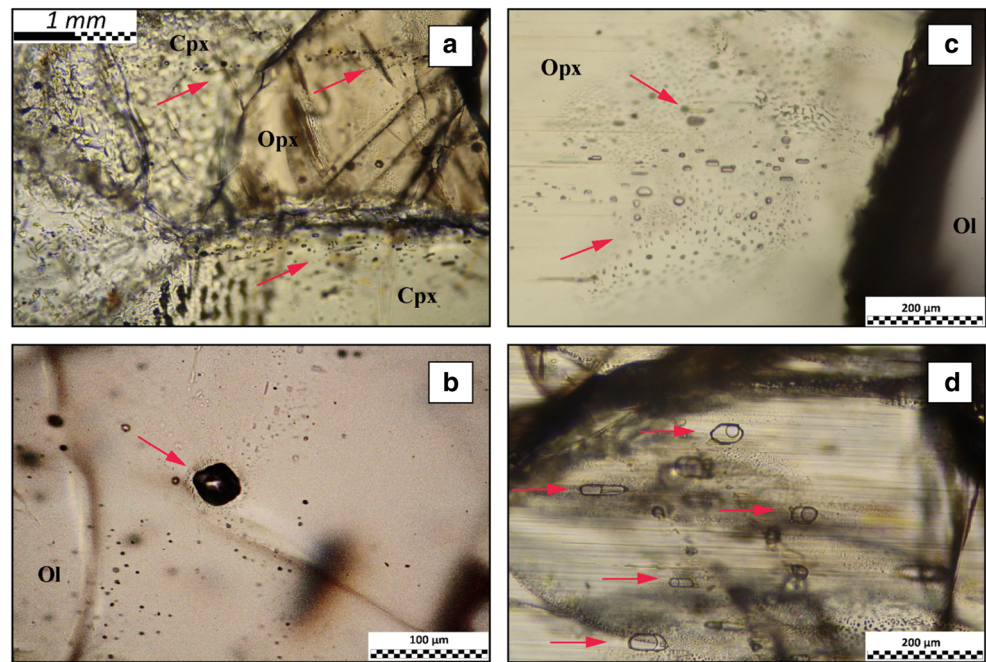
## Discussion

### Significance of fluid inclusion data

In mantle xenoliths, fluid inclusions represent either mantle metasomatic fluids, or fluids degassed by ascending basaltic magmas (cf., Andersen and Neumann 2001; Frezzotti and Touret 2014, and references therein). The chemical composition and the density of metasomatic and magmatic fluids can vary, since trapping can occur at different pressure and temperature conditions. Therefore, the chemical composition and the density distribution of fluid inclusions potentially provide important information on the depth of origin of mantle rocks, and/or on the episodes of magma storage at confined depths (cf., Andersen and Neumann 2001; Frezzotti and Peccerillo 2004; Hansteen and Klügel 2008).

The reliability of fluid inclusions as geobarometers relies on the isochoric principle, governed by the fluid equation of

**Fig. 5** Microphotographs of late type II fluid inclusions in LT and HT peridotites. **a** Intragranular trails (red arrows) in orthopyroxene porphyroclast and clinopyroxene. **b** Decrepitated fluid inclusions in an olivine porphyroclast, **c** Isolated cluster of fluid inclusions (red arrows). **d** Fluid inclusions distributed parallel to exsolution lamellae (red arrows) in an orthopyroxene porphyroclast



state (Roedder 1965). At trapping P-T conditions, the pressure of the fluid inside the inclusion equals the lithostatic pressure. During magma transport, however, the fluid undergoes evolving overpressure, since the external lithostatic or magmatic pressure becomes progressively lower than the original internal fluid pressure (Roedder 1984). If fluid overpressure exceeds the mechanical strength of the enclosing mineral, fluid inclusions undergo decrepitation and stretching, with partial-to-complete fluid loss, resulting in a density decrease.

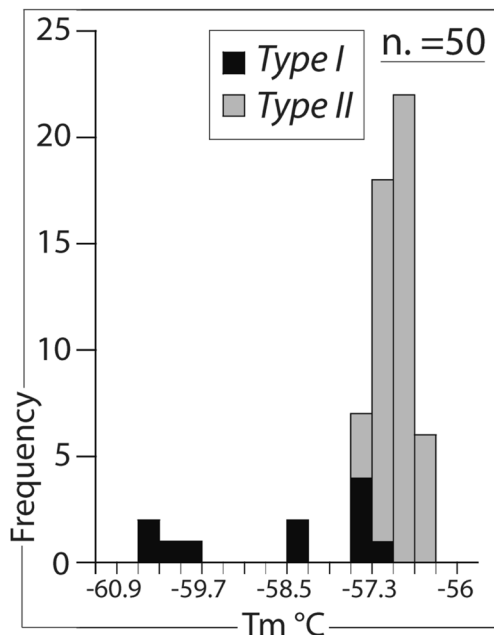


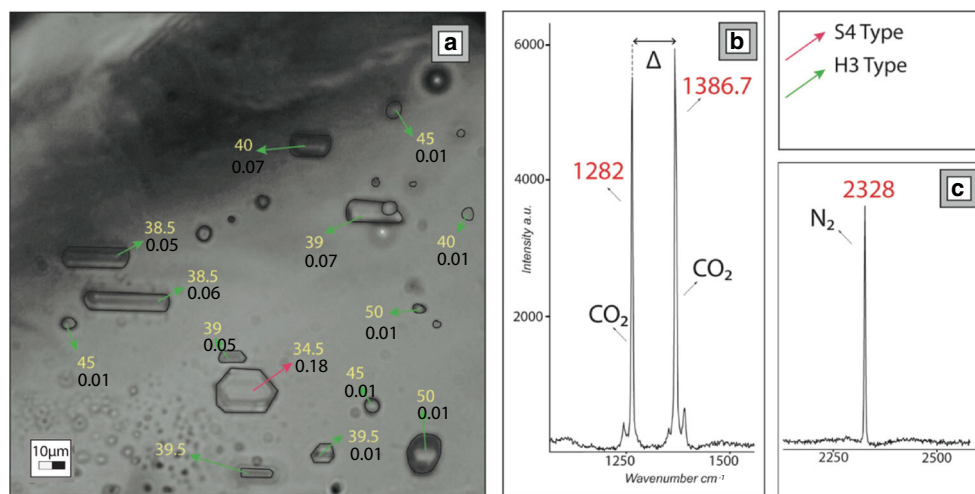
**Fig. 6** Histogram of CO<sub>2</sub> melting temperatures (T<sub>m</sub>) for type II fluid inclusions, and final CO<sub>2</sub> melting temperatures (T<sub>m</sub>) for type I fluid inclusions. n = number of measurements

Inclusion decrepitation and stretching depends on many variables, such as the composition, size, and distribution of the fluid inclusions, and the mechanical strength of the host mineral (e.g., Bodnar et al. 1989; Vityk and Bodnar 1998; Viti and Frezzotti 2001; Campione et al. 2015), but it does not reflect a decrease in magma decompression rates. A decrease in the ascent rate of magma—corresponding to magma rest episodes at confined depths—can be proposed if decrepitation and stretching reset inclusion densities to newly defined lower-pressure intervals and new episodes of fluid trapping occur (cf., Andersen and Neumann 2001; Frezzotti and Peccerillo 2004; Hansteen and Klügel 2008).

The present study reveals trapping of fluids during subsequent events. Type I inclusions represent the earlier and deeper fluids, as indicated by their distribution as small clusters or as crystallographically oriented groups in Ol I and exsolved Opx I of LT peridotites. Type I fluids are CO<sub>2</sub>-rich and contain variable amounts of N<sub>2</sub>, reaching 18 mol% in the densest inclusion (1.19 g/cm<sup>3</sup>). Their association with CO<sub>2</sub>-N<sub>2</sub> inclusions containing carbonates, sulfates, ± chlorides and spinel, and with carbonate-silicate glass microveins suggests an origin by immiscibility processes from a volatile-rich carbonate-silicate melt in the lithospheric mantle.

In the Canary Islands, mantle metasomatism by carbonatite or carbonate-silicate melts, enriched in volatiles and incompatible trace elements, has been described previously in the literature. In particular, carbonate-rich hydrous fluids or melts have been reported in peridotites from Tenerife, Lanzarote, and La Gomera (Frezzotti et al. 2002a, b; Neumann et al. 1995, 2002, 2004). Likewise, N<sub>2</sub> in CO<sub>2</sub> mantle fluids has been reported in peridotites from Lanzarote (Andersen et al. 1995). Notably, the presence of N<sub>2</sub> in CO<sub>2</sub>-rich inclusions was

**Fig. 7** **a** Composition ( $X_{N_2}$ ) and molar volume ( $\text{cm}^3/\text{mol}$ ) of type I  $\text{CO}_2\text{-N}_2$  fluid inclusions from a single cluster. Black numbers =  $X_{N_2}$ ; yellow numbers = molar volume ( $\text{cm}^3/\text{mol}$ ). **b**, **c** Raman spectra of  $\text{CO}_2$  and  $\text{N}_2$ ; ( $\Delta$ ) = distance of the Fermi doublet in  $\text{CO}_2$  Raman spectra. Red numbers report Raman vibrations in  $\text{cm}^{-1}$



also in this case revealed by Raman microspectroscopy, Raman being the only analytical technique able to detect trace amounts ( $\leq 0.1$  mol%) of  $\text{N}_2$  in fluid inclusions of small size.

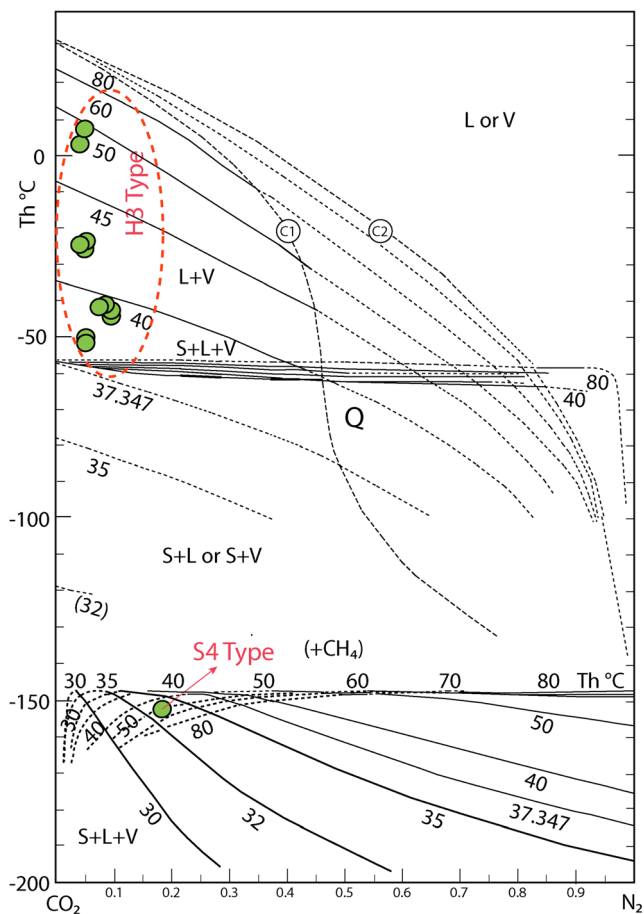


**Fig. 8** Isochore ( $\text{cm}^3/\text{mol}$ ) distribution in the T-X diagram for the  $\text{CO}_2\text{-N}_2$  system (modified from van den Kerkhof 1988 and Klemd et al. 1992). Measured phase transition sequences for S4 and H3 type I  $\text{CO}_2\text{-N}_2$  fluid inclusions of known composition allow calculation of molar volumes (green dots). Black numbers = fluid molar volumes in ( $\text{cm}^3/\text{mol}$ ); S = solid; L = liquid; V = vapor; Th = homogenization temperature

Metasomatic processes predate the onset of Canary magmatism (Neumann et al. 2004) and are unrelated to the ascent history of peridotites in the host lavas.

At a later stage, ingress of lower-density  $\text{CO}_2$  fluids occurred in both LT and HT peridotites. Type II inclusion distribution along intergranular trails is suggestive of fluid trapping by microfracturing of peridotites.  $\text{CO}_2$  density distribution intervals suggest two distinct fluid trapping and re-equilibration events (Fig. 10). In LT peridotites ( $T = 800\text{--}950$   $^\circ\text{C}$ ), density intervals are from 1.11 to  $0.99 \pm 0.01$   $\text{g}/\text{cm}^3$  and from 0.75 to  $0.65 \pm 0.01$   $\text{g}/\text{cm}^3$ , respectively (Fig. 12a). In peridotites equilibrated at higher temperatures (HT peridotites;  $T = 900\text{--}1100$   $^\circ\text{C}$ ),  $\text{CO}_2$  density distribution shows similar, but slightly lower values of 1.04 to  $0.91 \pm 0.01$  and 0.75 to  $0.65 \pm 0.01$   $\text{g}/\text{cm}^3$ , respectively (Fig. 12b).

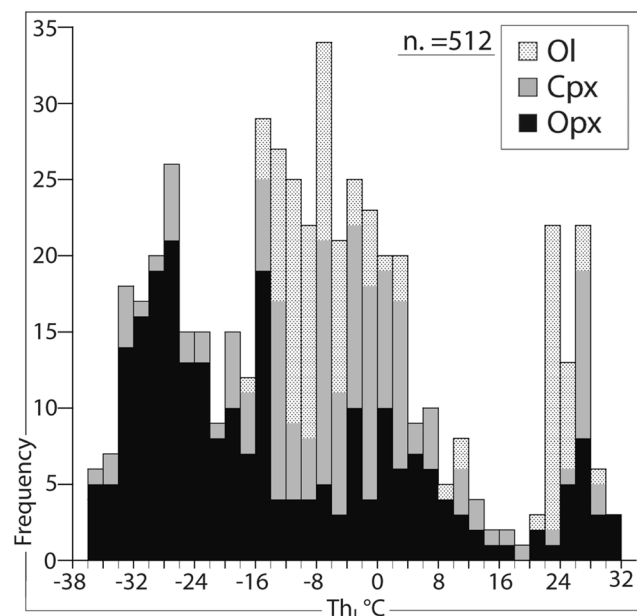


**Fig. 9** Histogram of  $\text{CO}_2$  homogenization temperatures ( $\text{Th}_L$ ) for Type II fluid inclusions. Ol = olivine; Opx = orthopyroxene; Cpx = clinopyroxene; n = number of measurements

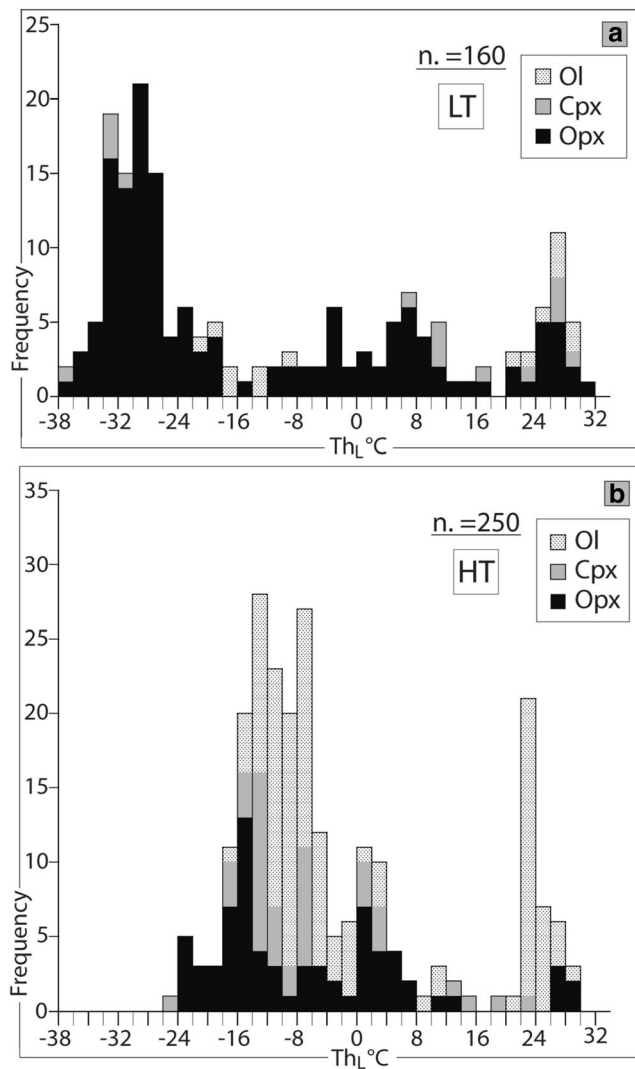
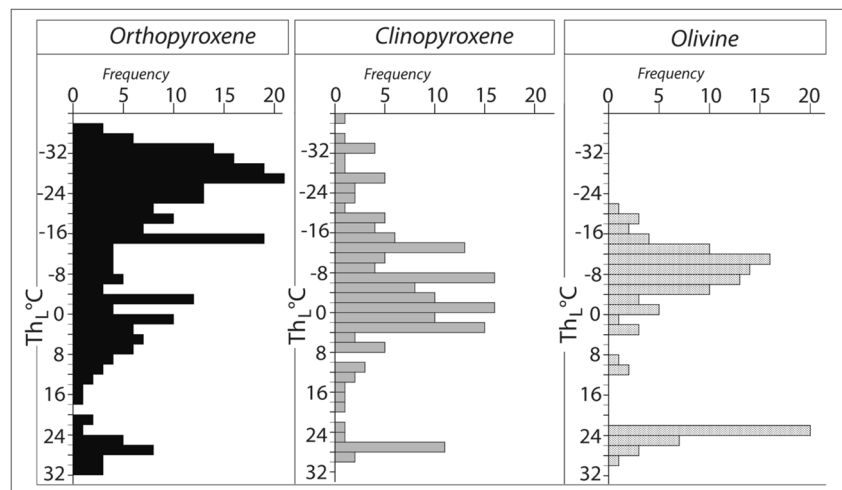


**Fig. 10** Histograms of CO<sub>2</sub> homogenization temperatures (ThL) for type II fluid inclusions in LT (a) and HT (b) peridotites. Abbreviations as in Fig. 9

The clear-cut variation of the chemistry of type II inclusions, which consist of pure CO<sub>2</sub>, suggests a different fluid

**Fig. 11** Histograms of CO<sub>2</sub> homogenization temperatures (ThL) for type II fluid inclusions showing data distribution in the different minerals. Abbreviations as in Fig. 9



origin, probably by degassing of magmas. Canary Island alkaline mafic magmas are carbon-rich and thus can begin to exsolve CO<sub>2</sub>-rich fluids at great pressures (> 1 GPa; Longpré et al. 2017) in the oceanic lithospheric mantle.

**Fluid inclusion geothermobarometry**

Once the composition and density of the fluids have been defined, temperatures need to be defined in order to calculate pressure conditions by fluid equations of state (Roedder 1965, 1984). In general, the temperature of the host lavas is taken as being representative of fluid trapping conditions in mantle xenoliths (cf., Andersen and Neumann 2001; Hansteen and Klügel 2008). In the present case, however, the preservation of type I inclusions only in LT peridotites and the density differences of type II CO<sub>2</sub> fluids in LT and HT peridotites suggest that xenoliths did not reach the same temperatures during ascent. For this reason, fluid trapping temperatures have been assumed based on mantle mineral geothermometry—800–950 °C for LT peridotites and 900–1100 °C for HT peridotites (Wells 1977, Brey and Köhler 1990 and Witt-Eickschen and Seck 1991). For each temperature interval, the highest value was selected assuming a component of increasing temperature caused by the ascent of mantle xenoliths in the basaltic host lavas.

The P-T distribution of Type I and II fluid isochores is shown in Fig. 13. The extremely high densities of type I CO<sub>2</sub>-N<sub>2</sub> fluids in LT peridotites (1.19 g/cm<sup>3</sup>; inclusion S4), correspond to trapping pressures of 1.80 ± 0.02 GPa at 950 °C (gray star in Fig. 13). This pressure is consistent with mineral geobarometry data, which indicate equilibration of peridotites in the mantle at 1.5–2.0 GPa for the same temperatures (Koebler and Brey 1990).

Conversely, trapping and/or re-equilibration of Type II CO<sub>2</sub> fluids occurred at lower pressures (Fig. 13) during two distinct episodes of magma rest at confined depths. In LT peridotites,

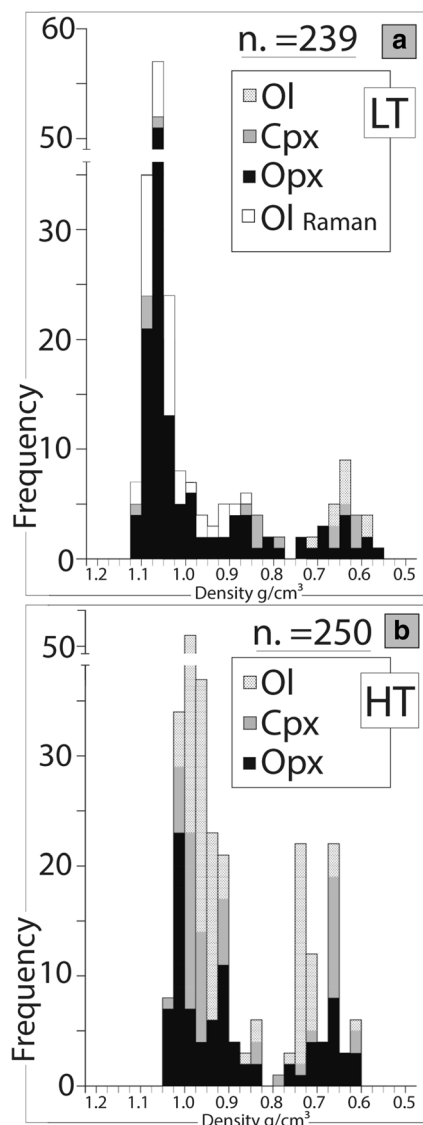


**Fig. 12** Distribution of  $\text{CO}_2$  density values for Type II fluid inclusions in LT (a) and HT (b) peridotites. See the text for the discussion. Abbreviations as in Fig. 9

isochore distributions for the denser type II inclusions correspond to pressures of between 1.00 and  $0.67 \pm 0.02$  GPa, at  $950^\circ\text{C}$  (green band in Fig. 13). In HT peridotites, type II fluid isochores indicate similar, though slightly lower, pressures of 0.89 to  $0.60 \pm 0.02$  GPa at  $1100^\circ\text{C}$  (blue band in Fig. 13). As illustrated in the P-T diagram in Fig. 13, largely overlapping isochoric bands confirm that type II inclusions in both LT and HT peridotites record a common deep magma storage region. The somewhat higher pressure values calculated for type II fluids in LT rocks (Fig. 13) indicate that fluid inclusions are better preserved in rocks equilibrated at lower temperatures.

A second  $\text{CO}_2$  trapping and re-equilibration event is defined by isochoric pressures (red isochore bands in Fig. 13) from 0.34 to  $0.26 \pm 0.02$  GPa at  $950^\circ\text{C}$  (type II inclusions in LT peridotites) and from 0.36 to  $0.28 \pm 0.02$  GPa at  $1100^\circ\text{C}$

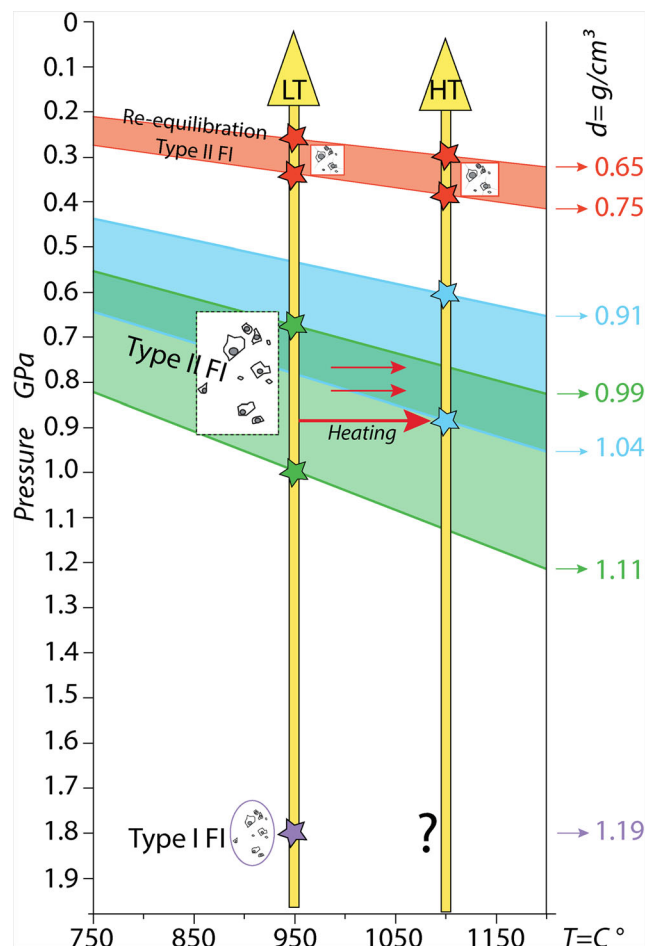


**Fig. 13**  $\text{CO}_2$  isochore ( $\text{g}/\text{cm}^3$ ) distribution in the P-T diagram for type I and type II fluid inclusions in LT and HT peridotites. Yellow arrows indicate the ascent path of LT and HT peridotites at the considered temperatures. The pink star indicates pressure conditions recorded by type I fluid inclusions in LT peridotites. Green and blue stars indicate pressures of deep trapping of type II  $\text{CO}_2$  fluids in LT and HT peridotites, respectively. Red stars indicate pressures of shallow trapping of type II  $\text{CO}_2$  fluids for LT and HT peridotites. Purple star indicates depth of origin of studied LT peridotites. Absence of Type I fluids in HT peridotites prevents a precise reconstruction of depths of origin (question mark).

(type II inclusions in HT peridotites). For both HT and LT peridotites, the isochore bands for type II inclusions differ from each other by only 0.02 GPa. This negligible pressure variation confirms the accuracy of the pressure estimates. This fluid trapping event corresponds to the last episode of magma rest before eruption.

### Recent magma transport dynamics beneath El Hierro

In order to model magma transport dynamics beneath El Hierro, having established the P-T conditions for fluid trapping, we need to calculate the corresponding depths. Fluid isochoric pressures have been converted into depths based on the relation:  $h = P/(g * d)$ , where  $h$  is the depth of origin or trapping of the fluids,  $P$  the lithostatic pressure,  $g$  the

acceleration due to gravity ( $9.81 \text{ m/s}^2$ ), and  $d$  the density of column-rocks. Main rock layer densities have been defined based on the following simplified stratigraphic reconstruction: a sequence of volcanic products and rocks with a density of  $2.5 \text{ g/cm}^3$  for the volcanic edifice (emergent and submarine height of island of about 4500 m; Acosta et al. 2005; Carracedo et al. 2012), a basaltic oceanic crust with a density of  $2.7 \text{ g/cm}^3$  (about 8500 m), and lithospheric peridotites with a density of  $3.3 \text{ g/cm}^3$ . Fluid inclusions studies in peridotite xenoliths show that polybaric magma transport characterizes the Rift Volcanism activity at about 40–30 ka. A schematic summary model, Figure 14, is discussed below.

The El Hierro Volcano is built on oceanic crust about 12–15 km in depth (Martinez-Arevalo et al. 2013) lying on a thick lithosphere of about 90–95 km (Dasgupta et al. 2010). Type I  $\text{CO}_2\text{-N}_2$  fluids associated with carbonate-silicate melts indicate that peridotites erupted from a source within the depth range of 60–65 km ( $P = 1.80 \pm 0.02 \text{ GPa}$ ; gray star in Fig. 14) within the lower lithospheric mantle. As discussed in the previous sections, geochemical characteristics of the peridotites beneath the Canary Islands point to mantle metasomatism by carbonate-rich melts (e.g., Neumann et al. 2004). The presence of oceanic carbonatites of Oligocene to Lower Miocene age in Fuerteventura (Lebas et al. 1986) provides further support to a carbonate enriched lithospheric mantle. Type II fluid inclusions were formed during magma rest at confined depths for a period of time sufficient to allow  $\text{CO}_2$  trapping. Fluid density distribution identifies two main magma accumulation regions. The deeper one is located in the shallow lithospheric mantle at depths of 37 to 22 km (Fig. 14). This mantle magma reservoir served as the main storage area for the volcano and fed a smaller reservoir located at 10–12 km depth (Fig. 14) near the base of the oceanic crust, from where mafic magmas erupted.

Magma storage at crustal conditions does not appear to have been long-lived. The preservation of high-density type I and II inclusions suggests that mafic magmas arrived at the lower oceanic crust reservoirs shortly (a matter of days) before eruption. Longer magma stagnation would have caused the complete resetting of fluid inclusion densities to shallower ambient pressures (Wanamaker and Evans 1989; Hansteen and Klügel 2008).

The lithospheric mantle reservoir revealed by this present study is particularly thick, of the order of 15 km (i.e., from 37 to 22 km depth). Thus, magma is likely to have been stored in a series of interconnected pockets distributed over this large depth interval (Fig. 14). Similar magma accumulation as vertically stacked small reservoirs has been previously proposed for Kilauea and Piton de la Fournaise (Decker et al. 1987; Ryan 1988; Voog et al. 1999; Michon et al. 2015). In these volcanoes, deep magma transport dynamics have been interpreted as the result of magma storage in the lithospheric mantle, either through a microfracture network system over a

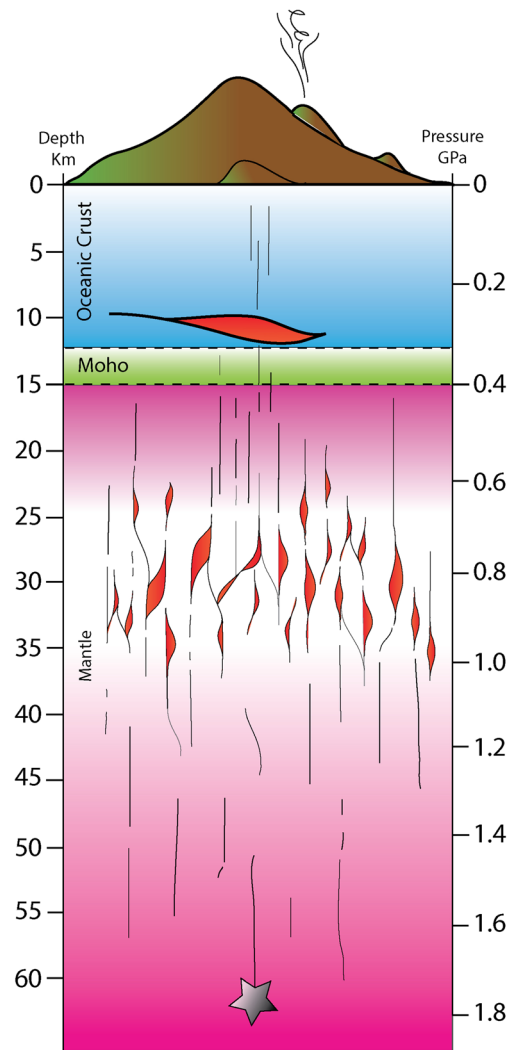


**Fig. 14** Proposed model for the magma plumbing system of El Hierro Volcano at 40–30 ka. A deep-seated reservoir is located in the shallow lithospheric mantle at depths of approximately 37 to 22 km. A short-lived shallower reservoir is located in the lower oceanic crust at 12–10 km. See the text for the discussion. Black star = source of mantle xenoliths

large depth interval (e.g., magma-fracturing by  $\text{CO}_2$  degassing; Shaw 1980a, 1980b; Pollard et al. 1983; Decker et al. 1987) or in a porous mantle matrix (Gudmundsson 1987). Partially molten mantle storage regions where magma is stored and undergoes degassing are considered to be long lived (Shaw 1980a, b; Pollard et al. 1983; Decker et al. 1987); although their formation is still not unanimously agreed on, they have been proposed in regions of oceanic intraplate volcanism characterized by slow magma supply (e.g., Shaw 1980a, b), which would be in agreement with the low long-term magma rate of the El Hierro Volcano ( $0.12\text{--}0.13 \text{ km}^3/\text{ka}$ ; Carracedo 1999).

The proposed polybaric magma storage system appears to agree with magma transport dynamics reconstructed for the 2011–2012 eruption (e.g., Meletlidis et al. 2012; Becerril et al. 2013b; González et al. 2013; Martí et al. 2013a, b; Longpré et al. 2014; Klügel et al. 2015). Therefore, it seems that the

magma plumbing system has been essentially the same for the last 30–40 ka. For instance, the upper limit of the deep magma storage region identified by fluid inclusions at approximately 22 km (Fig. 14) corresponds to the depth of the pre-sin-eruptive earthquake hypocenters (20–25 km) interpreted to reflect the magma source that fed the 2011–2012 eruption (e.g., López et al. 2012; Martí et al. 2013a, b; Longpré et al. 2014). Furthermore, storage of the 2011–2012 magma in the lower oceanic crust is likewise considered to have been ephemeral, not developing into a long-term reservoir (e.g., Becerril et al. 2013b; Longpré et al. 2014; Martí et al. 2013a, b; Klügel et al. 2015). These authors further interpreted the pre-eruptive lateral magma migration of about 15–20 km from the north towards the south as evidence of sill propagation. Although fluid inclusion data cannot resolve horizontal magma movements, temporary magma stagnation in a region of neutral buoyancy, such as the lower crust, might have favored lateral transport.

In oceanic islands, magma pathways are established in the early growth stages but evolve over time, along with the volcano. Our model does not indicate storage of magmas directly beneath the Moho (i.e., 15 to 25 km) for present rift volcanism activity, as previously proposed by Stroncik et al. (2009) based on clinopyroxene-melt geobarometric data in prehistorical lavas of undetermined age. Confinement of magmas at about 7–10 km below the geophysical interface of the oceanic crust and the mantle (12–15 km; Fig. 14) can be tentatively interpreted as an indication of magma underplating below El Hierro. At the nearby island of La Palma, progressive deepening of the magma plumbing system, induced by up to 10 km of magma underplating, has been recently proposed by Barker et al. (2015). Similarly, geophysical data from the Canary Islands (Carracedo et al. 2015) point to underplating beneath Tenerife and Gran Canaria at the same depth interval. In this respect, further studies of fluid inclusions in mantle xenoliths in lavas of older volcanic cycles of El Hierro should make it possible to trace the evolution of magma transport beneath this volcano over its entire history.

## Summary and conclusions

Our present study focuses on the reconstruction of a model of the recent magma dynamics beneath El Hierro Island based on combined fluid inclusion and mineral geothermobarometry studies in mantle xenoliths entrained in lavas of the Rift Volcanism activity (40–30 ka). Two distinct fluid phases have been characterized by microthermometry and Raman microspectroscopy. Type I CO<sub>2</sub>-N<sub>2</sub> mantle metasomatic fluids were trapped at pressures of  $1.80 \pm 0.02$  GPa, or about 60–65 km depth, before xenolith entrainment in the host lava. Type II CO<sub>2</sub> fluids, probably degassed from host mafic magmas, reveal two discrete magma accumulation regions:

the first in the lithospheric mantle, from 1 to  $0.60 \pm 0.02$  GPa, or 37 to 22 km depth, and a second in the lower oceanic crust, from 0.34 to  $0.21 \pm 0.02$  GPa, or 12 to 10 km depth. The deeper accumulation region is interpreted as a stacked system of interconnected small magma pockets distributed in the lithospheric mantle beneath El Hierro, which fed a temporary lower crustal storage region.

Models of the internal structure of active volcanoes are important for constraining reliable monitoring strategies and forecasting volcanic eruptions (e.g. Peccerillo et al. 2006; Scandone et al. 2007; Becerril et al. 2015). This fluid inclusion study produces a potentially accurate model for the El Hierro Volcano, since magma migration within the plumbing system is comparable to that registered during the 2011–2012 eruption. The implications are that magma migration from the deep reservoir should be monitored as a precursor to magma rise towards the surface and hence eruption. This could be achieved by considering both mantle seismicity, conceivably connected with upward migration of earthquake hypocenters, and changes in the gravity field as a consequence of magma migration within the plumbing system.

**Acknowledgements** This paper is a part of E.O.'s Ph.D. thesis. We are grateful to L. Becerril, M. Campione, F. Lucchi, N. Malaspina, and V. Zanon for the helpful discussions. We acknowledge A. Risplendente for the assistance during microprobe analyses. Editorial handling by A. Harris and V. Kamenetsky, and reviews by F. Deegan, T. Hansteen, and an anonymous reviewer have considerably improved the manuscript. Funding was provided by the University of Milan Bicocca, FAR-2015 to M.L.F. and I.M.V. Raman facilities were provided by the Interdepartmental Center "G. Scansetti" for studies on asbestos and other toxic particulates at the University of Turin.

## References

- Acosta J, Uchupi E, Muñoz A, Herranz P, Palomo C, Ballesteros M, Working ZE (2005) Geologic evolution of the Canary Islands of Lanzarote, Fuerteventura, Gran Canaria and La Gomera and comparison of landslides at these islands with those at Tenerife, La Palma and El Hierro. *Mar Geophys Res* 24:1–40
- Andersen T, Neumann ER (2001) Fluid inclusions in mantle xenoliths. *Lithos* 55:301–332
- Andersen T, Burke EJ, Neumann ER (1995) Nitrogen-rich fluid in the upper mantle: fluid inclusions in spinel dunite from Lanzarote, Canary Islands. *Contrib Mineral Petrol* 120:20–28
- Anguita F, Hernán F (1975) A propagating fracture model versus a hot spot origin for the Canary Islands. *Earth Planet Sci Lett* 27:11–19
- Anguita F, Hernán F (2000) The Canary Islands origin: a unifying model. *J Volcanol Geotherm Res* 103:1–26
- Araña V, Ortiz R (1991) The Canary Islands: tectonics, magmatism and geodynamic framework. In: Kampunzu A, Lubala R (eds) *Magmatism in extensional structures setting: the Phanerozoic African Plate*. Springer Verlag, pp. 209–249
- Bakker RJ (2003) Package FLUIDS1. Computer programs for analysis of fluid inclusion data and for modelling bulk fluid properties. *Chem Geol* 194:3–23

- Barker AK, Troll VR, Carracedo JC, Nicholls PA (2015) The magma plumbing system for the 1971 Teneguía eruption on La Palma, Canary Islands. *Contrib Mineral Petrol* 170:5–6
- Becerril L, Cappello A, Galindo I, Neri M, Del Negro C (2013a) Spatial probability distribution of future volcanic eruptions at El Hierro Island (Canary Islands, Spain). *J Volcanol Geotherm Res* 257:21–30
- Becerril L, Galindo I, Gudmundsson A, Morales JM (2013b) Depth of origin of magma in eruptions. *Sci Rep* 3:1–6. <https://doi.org/10.1038/srep02762>
- Becerril L, Galindo I, Martí J, Gudmundsson A (2015) Three-armed rifts or masked radial pattern of eruptive fissures? The intriguing case of El Hierro Volcano (Canary Islands). *Tectonophysics* 647:33–47
- Bertagnini A, Métrich N, Landi P, Rosi M (2003) Stromboli volcano (Aeolian archipelago, Italy): an open window on the deep-feeding system of a steady state basaltic volcano. *J Geophys Res* 108:2336–2342
- Bodnar RJ (2003) Introduction to aqueous-electrolyte fluid inclusions. In: Samson I, Anderson A, Marshall D (eds) *Fluid inclusions: analysis and interpretation*. Mineral Ass Canada Short Course Series 32, pp 81–100
- Bodnar RJ, Binns PR, Hall DL (1989) Synthetic fluid inclusions—VI. Quantitative evaluation of the decrepitation behaviour of fluid inclusions in quartz at one atmosphere confining pressure. *J Metamorph Geol* 7:229–242
- Brey GP, Köhler T (1990) Geothermobarometry in four-phase lherzolites II. New thermobarometers, and practical assessment of existing thermobarometers. *J Petrol* 31:1353–1378
- Campione M, Malaspina N, Frezzotti ML (2015) Threshold size for fluid inclusion decrepitation. *J Geophys Res Solid Earth* 120:7396–7402
- Carracedo JC (1999) Growth, structure, instability and collapse of Canarian volcanoes and comparisons with Hawaiian volcanoes. *J Volcanol Geotherm Res* 94:1–19
- Carracedo JC, Day S, Guillou H, Rodríguez Badiola E, Canas JA, Pérez Torrado FJ (1998) Hotspot volcanism close to a passive continental margin: the Canary Islands. *Geol Mag* 135:591–604
- Carracedo JC, Badiola ER, Guillou H, de La Nuez J, Pérez Torrado FJ (2001) Geology and volcanology of La Palma and El Hierro (Canary Islands). *Estudios Geol* 57:175–273
- Carracedo JC, Perez-Torrado FJ, Rodriguez-Gonzalez A, Fernandez-Turiel JL, Klügel A, Troll VR, Wiesmaier S (2012) The ongoing volcanic eruption of El Hierro, Canary Islands. *Eos* 93:89–90
- Carracedo JC, Troll VR, Zaczek K, Rodriguez-Gonzalez A, Soler V, Deegan FM (2015) The 2011–2012 submarine eruption off El Hierro, Canary Islands: new lessons in oceanic island growth and volcanic crisis management. *Earth-Sci Rev* 150:168–200
- Dasgupta R, Jackson MG, Lee C-TA (2010) Major element chemistry of ocean island basalts—conditions of mantle melting and heterogeneity of mantle source. *Earth Planet Sci Lett* 289:377–392
- De Vivo B, Frezzotti ML, Lima A, Trigila R (1988) Spinel lherzolite nodules from Oahu Island (Hawaii): a fluid inclusion study. *Bull Minéral* 111:307–319
- Decker RW, Wright TL, Stauffer, S (1987). *Volcanism in Hawaii*. US Gov Printing Office, p 1606
- Duggen S, Hoernle K, Hauff F, Klügel A, Bouabdellah M, Thirlwall MF (2009) Flow of canary mantle plume material through a subcontinental lithospheric corridor beneath Africa to the Mediterranean. *Geology* 37:283–286
- Duschek W, Kleinrahm R, Wagner W (1990) Measurement and correlation of the (pressure, density, temperature) relation of carbon dioxide I. The homogeneous gas and liquid regions in the temperature range from 217 K to 340 K at pressures up to 9 MPa. *J Chem Thermod* 22: 827–840
- Frey FA, Prinz M (1978) Ultramafic inclusions from San Carlos, Arizona: petrologic and geochemical data bearing on their petrogenesis. *Earth Planet Sci Lett* 38:129–176
- Frezzotti ML, Peccerillo A (2004) Fluid inclusion and petrological studies elucidate reconstruction of magma conduits. *Eos* 85:157–160
- Frezzotti ML, Touret JL (2014) CO<sub>2</sub>, carbonate-rich melts, and brines in the mantle. *Geosci Front* 5:697–710
- Frezzotti ML, De Vivo B, Clocchiatti R (1991) Melt-mineral-fluid interactions in ultramafic nodules from alkaline lavas of Mount Etna (Sicily, Italy): melt and fluid inclusion evidence. *J Volcanol Geotherm Res* 47:209–219
- Frezzotti ML, Touret JL, Lustenhouwer WJ, Neumann ER (1994) Melt and fluid inclusions in dunite xenoliths from La Gomera, Canary Islands: tracking the mantle metasomatic fluids. *Eur J Mineral* 6: 805–817
- Frezzotti ML, Andersen T, Neumann ER, Simonsen SL (2002a) Carbonatite melt–CO<sub>2</sub> fluid inclusions in mantle xenoliths from Tenerife, Canary Islands: a story of trapping, immiscibility and fluid–rock interaction in the upper mantle. *Lithos* 64:77–96
- Frezzotti ML, Touret JL, Neumann ER (2002b) Ephemeral carbonate melts in the upper mantle. *Eur J Mineral* 14:891–904
- Frezzotti ML, Tecce F, Casagli A (2012) Raman spectroscopy for fluid inclusion analysis. *J Geochem Explor* 112:1–20
- Füster J (1975) Las Islas Canarias: un ejemplo de evolución temporal y espacial del vulcanismo oceánico. *Estud Geol* 31:439–463
- Garrabos Y, Tufeu R, Le Neindre B, Zalczer G, Beysens D (1980) Rayleigh and Raman scattering near the critical point of carbon dioxide. *J Chem Phys* 72:4637–4651
- Gee MJR, Masson DG, Watts AB, Mitchell NC (2001) Offshore continuation of volcanic rift zones, El Hierro, Canary Islands. *J Volcanol Geotherm Res* 105:107–119
- Geyer A, Martí J (2010) Tectonophysics the distribution of basaltic volcanism on Tenerife, Canary Islands: implications on the origin and dynamics of the rift systems. *Tectonophysics* 483:310–326
- González PJ, Samsonov SV, Pepe S, Tiampo KF, Tizzani P, Casu F, Sansosti E (2013) Magma storage and migration associated with the 2011–2012 El Hierro eruption: implications for crustal magmatic systems at oceanic island volcanoes. *J Geophys Res Solid Earth* 118: 4361–4377
- Gudmundsson A (1987) Geometry, formation and development of tectonic fractures on the Reykjanes Peninsula, southwest Iceland. *Tectonophysics* 139:295–308
- Guillou H, Carracedo JC, Torrado FP, Badiola ER (1996) K-Ar ages and magnetic stratigraphy of a hotspot-induced, fast grown oceanic island: El Hierro, Canary Islands. *J Volcanol Geotherm Res* 73:141–155
- Hansteen TH, Klügel A, (2008) Fluid inclusion thermobarometry as a tracer for magmatic processes. In: Putirka KD, Tepley FJ (eds) *Reviews in Mineralogy Min Soc Amer* 149:143–177
- Hansteen TH, Andersen T, Neumann ER, Jelsma H (1991) Fluid and silicate glass inclusions in ultramafic and mafic xenoliths from Hierro, Canary Islands: implications for mantle metasomatism. *Contrib Mineral Petrol* 107:242–254
- Hansteen TH, Klügel A, Schmincke HU (1998) Multi-stage magma ascent beneath the Canary Islands: evidence from fluid inclusions. *Contrib Mineral Petrol* 132:48–64
- Hoernle KAJ (1998) Geochemistry of Jurassic oceanic crust beneath Gran Canaria (Canary Islands): implications for crustal recycling and assimilation. *J Petrol* 39:859–880
- Hoernle K, Schmincke HU (1993) The role of partial melting in the 15-Ma geochemical evolution of Gran Canaria: a blob model for the Canary hotspot. *J Petrol* 34:599–626
- Holloway JR (1977). Fugacity and activity of molecular species in supercritical fluids. In: Fraser DG (ed) *Thermodynamics in geology*, Dordrecht-Holland, pp 161–181
- Holloway JR (1981) Compositions and volumes of supercritical fluids. In: Hollister L, Crawford ML (eds) *Fluid inclusions: application to petrology*. Min Soc Canada Short Course Handbook, pp. 13–38
- IGME (2010a) Mapa Geológico de España, Escala 1:25.000. Isla de El Hierro. Hoja 1105- II, Valverde, pp. 96

- IGME (2010b) Mapa Geológico de España, Escala 1:25.000. Isla de El Hierro. Hoja 1105- III, Sabinosa, pp, 71
- IGME (2010c) Mapa Geológico de España, Escala 1:25.000. Isla de El Hierro. Hoja 1105- IV, Frontera, pp, 84
- IGME (2010d) Mapa Geológico de España, Escala 1:25.000. Isla de El Hierro. Hoja 1108- I/II, La Restinga, pp, 55
- Kawakami Y, Yamamoto J, Kagi H (2003) Micro-Raman densimeter for CO<sub>2</sub> inclusions in mantle-derived minerals. *Appl Spectrosc* 57: 1333–1339
- Klemm R, van den Kerkhof AM, Horn EE (1992) High-density CO<sub>2</sub>-N<sub>2</sub> inclusions in eclogite-facies metasediments of the Münchberg gneiss complex, SE Germany. *Contrib Mineral Petrol* 111:409–419
- Klügel A, Hansteen TH, Galipp K (2005) Magma storage and underplating beneath Cumbre Vieja Volcano, La Palma (Canary Islands). *Earth Planet Sci Lett* 236:211–226
- Klügel A, Longpré MA, García-Cañada L, Stix J (2015) Deep intrusions, lateral magma transport and related uplift at ocean island volcanoes. *Earth Planet Sci Lett* 43:140–149
- Koehler TP, Brey GP (1990) Calcium exchange between olivine and clinopyroxene calibrated as a geothermobarometer for natural peridotites from 2 to 60 kb with applications. *Geochim Cosmochim Acta* 54:2375–2388
- Lebas MJ, Rex DC, Stillman CJ (1986) The early magmatic chronology of Fuerteventura, Canary Islands. *Geol Mag* 123:287–298
- Longpré MA, Chadwick JP, Wijbrans J, Iping R (2011) Age of the El Golfo debris avalanche, El Hierro (Canary Islands): new constraints from laser and furnace 40Ar/ 39Ar dating. *J Volcanol Geotherm Res* 203:76–80
- Longpré MA, Klügel A, Diehl A, Stix J (2014) Mixing in mantle magma reservoirs prior to and during the 2011–2012 eruption at El Hierro, Canary Islands. *Geology* 42:315–318
- Longpré MA, Stix J, Klügel A, Shimizu N (2017) Mantle to surface degassing of carbon- and sulphur-rich alkaline magma at El Hierro, Canary Islands. *Earth Planet Sci Lett* 460:268–280
- López C, Blanco MJ, Abella R, Brenes B, Cabrera Rodríguez VM, Casas B, Domínguez Cerdeña I, Felpeto A, Fernández de Villalta M, del Fresno C, García O, García-Arias MJ, García-Cañada L, Gomis Moreno A, González-Alonso E, Guzmán Pérez J, Iribarren F, López-Díaz R, Luengo-Oroz N, Meletlidis S, Moreno M, Moure D, Pereda de Pablo J, Rodero E, Romero E, Sainz-Maza S, Sente Domingo MA, Torres PA, Trigo P, Villasante-Marcos V (2012) Monitoring the volcanic unrest of El Hierro (Canary Islands) before the onset of the 2011–2012 submarine eruption. *Geophys Res Lett* 39:L13303
- Lustrino M, Wilson M (2007) The circum-Mediterranean anorogenic Cenozoic igneous province. *Earth-Sci Rev* 81:1–65
- Marinoni LB, Gudmundsson A (2000) Dykes, faults and palaeostresses in the Teno and Anaga massifs of Tenerife (Canary Islands). *J Volcanol Geotherm Res* 103:83–103
- Marinoni LB, Pasquaré G (1994) Tectonic evolution of the emergent part of a volcanic ocean island: Lanzarote, Canary Islands. *Tectonophysics* 239:111–137
- Martí J, Castro A, Rodríguez C, Costa F, Carrasquilla S, Pedreira R, Bolos X (2013a) Correlation of magma evolution and geophysical monitoring during the 2011–2012 El Hierro (Canary Islands) submarine eruption. *J Petrol* 54:1349–1373
- Martí J, Pínel V, López C, Geyer A, Abella R, Tárraga M, Rodríguez C (2013b) Causes and mechanisms of the 2011–2012 El Hierro (Canary Islands) submarine eruption. *J Geophys Res Solid Earth* 118:823–839
- Martínez-Arevalo C, Mancilla FD, Helffrich G, García A (2013) Seismic evidence of a regional sublithospheric low velocity layer beneath the Canary Islands. *Tectonophysics* 608:586–599
- Masson DG (1996) Catastrophic collapse of the volcanic island of Hierro 15 ka ago and the history of landslides in the Canary Islands. *Geology* 24:231–234
- Masson DG, Watts B, Gee MJR, Urgeles R, Mitchell NC, Le Bas TP, Canals M (2002) Slope failures on the flanks of the western Canary Islands. *Earth-Sci Rev* 57:1–35
- Masson DG, Harbitz CB, Wynn RB, Pedersen G, Løvholt F (2006) Submarine landslides: processes, triggers and hazard prediction. *Philos Transact A Math Phys Eng Sci* 364:2009–2039
- Meletlidis S, Roberto A, Di Pompilio M, Bertagnini A, Iribarren I, Felpeto A, Oriano CD (2012) Xenopumices from the 2011–2012 submarine eruption of El Hierro (Canary Islands, Spain): constraints on the plumbing system and magma ascent. *Geophys Res Lett* 39:1–6
- Michon L, Ferrazzini V, Di Muro A, Villeneuve N, Famin V (2015) Rift zones and magma plumbing system of Piton de la Fournaise Volcano: how do they differ from Hawaii and Etna? *J Volcanol Geotherm Res* 303:112–129
- Morgan DJ, Jerram DA, Chertkoff DG, Davidson JP, Pearson DG, Kronz A, Nowell GM (2007) Combining CSD and isotopic microanalysis: magma supply and mixing processes at Stromboli Volcano, Aeolian Islands, Italy. *Earth Planet Sci Lett* 260:419–431
- Neumann E (1990) Ultramafic and mafic xenoliths from Hierro, Canary Islands: evidence for melt infiltration in the upper mantle. *Contrib Mineral Petrol* 106:1689–1699
- Neumann ER, Wulff-Pedersen E, Johnsen K, Andersen T, Krogh E (1995) Petrogenesis of spinel harzburgite and dunite suite xenoliths from Lanzarote, eastern Canary Islands: implications for the upper mantle. *Lithos* 35:83–107
- Neumann ER, Wulff-Pedersen E, Pearson NJ, Spencer EA (2002) Mantle xenoliths from Tenerife (Canary Islands): evidence for reactions between mantle peridotites and silicic carbonatite melts inducing Ca metasomatism. *J Petrol* 43:825–857
- Neumann ER, Griffin WL, Pearson NJ, O'Reilly SY (2004) The evolution of the upper mantle beneath the Canary Islands: information from trace elements and Sr isotope ratios in minerals in mantle xenoliths. *J Petrol* 45:2573–2612
- Peccerillo A, Frezzotti ML, De Astis G, Ventura G (2006) Modeling the magma plumbing system of Vulcano (Aeolian Islands, Italy) by integrated fluid-inclusion geobarometry, petrology, and geophysics. *Geology* 34:17–20
- Pollard DD, Delaney PT, Duffield WA, Endo ET, Okamura AT (1983) Surface deformation in volcanic rift zones. *Tectonophysics* 94:541–584
- Robertson AHF, Stillman CJ (1979) Submarine volcanic and associated sedimentary rocks of the Fuerteventura Basal Complex, Canary Islands. *Geol Mag* 116:203–214
- Roedder E (1965) Liquid CO<sub>2</sub> inclusions in olivine-bearing nodules and phenocrysts from basalts. *Am Mineral* 50:20–40
- Roedder E (1983) Geobarometry of ultramafic xenoliths from Loihi Seamount, Hawaii, on the basis of CO<sub>2</sub> inclusions in olivine. *Earth Planet Sci Lett* 66:369–379
- Roedder E (1984) Fluid inclusions. Roedder, E. (1984) Fluid inclusions. *Mineral Soc America Rev in Mineral* 12, pp 644
- Rosso KM, Bodnar RJ (1995) Detection limits of CO<sub>2</sub> in fluid inclusions using microthermometry and laser Raman spectroscopy and the spectroscopic characterization of CO<sub>2</sub>. *Geochim Cosmochim Acta* 59:3961–3975
- Ryan MP (1987) Neutral buoyancy and the mechanical evolution of magmatic systems. In: Mysen BO (ed) *Magmatic processes: physicochemical principles*. University Park, Texas, The Geochem Soc, pp 259–287
- Ryan MP (1988) Structure of active magmatic systems' Kilauea Volcano, Hawaii. *J Geophys Res* 93:4213–4248
- Scandone R, Cashman KV, Malone SD (2007) Magma supply, magma ascent and the style of volcanic eruptions. *Earth Planet Sci Lett* 253: 513–529
- Schmincke HU (1982) Volcanic and chemical evolution of the Canary Islands. In: VonRad U, Hinz K, Sarnthein M and Seibol E (eds)

- Geology of the northwest African continental margin. Springer Verlag, New York, pp 273–306
- Schwarz S, Klügel A, Wohlgemuth-Ueberwasser C (2004) Melt extraction pathways and stagnation depths beneath the Madeira and Desertas rift zones (NE Atlantic) inferred from barometric studies. *Contrib Mineral Petrol* 147:228–240
- Shaw HR (1980a) The fracture mechanisms of magma transport from the mantle to the surface. In: Hargraves RB (ed) *Physics of magmatic processes*. Princeton University Press, Princeton, pp 201–264
- Shaw HR (1980b) The fracture mechanisms of magma transport from the mantle to the surface. *Phys Magmat Processes* 64:201–264
- Sparks RSJ (2003) Forecasting volcanic eruptions. *Earth Planet Sci Lett* 210:1–15
- Stroncik NA, Klügel A, Hansteen TH (2009) The magmatic plumbing system beneath El Hierro (Canary Islands): constraints from phenocrysts and naturally quenched basaltic glasses in submarine rocks. *Contrib Mineral Petrol* 157:593–607
- Ulmer P (1986) NORM-program for cation and oxygen mineral norms. Computer Library, Institut für Mineralogie und Petrographie, ETH-Zentrum, Zürich, Switzerland
- van den Kerkhof AM (1988) The system CO<sub>2</sub>–CH<sub>4</sub>–N<sub>2</sub> in fluid inclusions: theoretical modelling and geological applications. PhD Dissertation, Amsterdam Free University, pp. 206
- Viti C, Frezzotti ML (2000) Re-equilibration of glass and CO<sub>2</sub> inclusions in xenolith olivine: a TEM study. *Am Mineral* 85:1390–1396
- Viti C, Frezzotti ML (2001) Transmission electron microscopy applied to fluid inclusion investigations. *Lithos* 55:125–138
- Vityk MO, Bodnar RJ (1998) Statistical microthermometry of synthetic fluid inclusions in quartz during decompression re-equilibration. *Contrib Mineral Petrol* 132:149–162
- Voog DB, Palomé SP, Hirn A, Charvis P, Gallart J, Rousset D, Perroud H (1999) Vertical movements and material transport during hotspot activity: seismic reflection profiling offshore La Réunion. *J Geophys Res* 104:2855–2874
- Wanamaker BJ, Evans B (1989) Mechanical re-equilibration of fluid inclusions in San Carlos olivine by power-law creep. *Contrib Mineral Petrol* 102:102–111
- Wang CH, Wright RB (1973) Effect of density on the Raman scattering of molecular fluids. I. A detailed study of the scattering polarization, intensity, frequency shift, and spectral shape in gaseous N<sub>2</sub>. *J Chem Phys* 59:1706–1712
- Wells PR (1977) Pyroxene thermometry in simple and complex systems. *Contrib Mineral Petrol* 62:129–139
- Witt-Eickschen G, Seck HA (1991) Solubility of Ca and Al in orthopyroxene from spinel peridotite: an improved version of an empirical geothermometer. *Contrib Mineral Petrol* 106:431–439
- Zaczek K, Troll VR, Cachao M, Ferreira F, Deegan FM, Carracedo JC, Meade FC, Burchardt S (2015) Nannofossils in 2011 El Hierro eruptive products reinstate plume model for Canary Islands. *Sci Rep* 5:7945. <https://doi.org/10.1038/srep07945>
- Zanon V, Frezzotti ML (2013) Magma storage and ascent conditions beneath Pico and Faial islands (Azores archipelago): a study on fluid inclusions. *Geochem Geophys Geosyst* 14:3494–3514
- Zanon V, Frezzotti ML, Peccerillo A (2003) Magmatic feeding system and crustal magma accumulation beneath Vulcano Island (Italy): evidence from CO<sub>2</sub> fluid inclusions in quartz xenoliths. *J Geophys Res* 108:2298. <https://doi.org/10.1029/2002JB002140>